Size-dependent magnetic ordering and spin dynamics in DyPO$_4$ and GdPO$_4$ nanoparticles

Marco Evangelisti,[1,*] Tibi G. Sorop,[2] Oleg N. Bakharev,[2] Dirk Visser,[3,4] Adrian D. Hillier,[3] Juan J. Alonso,[5] Markus Haase,[6] Lynn A. Boatner,[7] and L. Jos de Jongh[2,†]

[1]*Instituto de Ciencia de Materiales de Aragón (ICMA), CSIC-Universidad de Zaragoza, Departamento de Física de la Materia Condensada, E-50009 Zaragoza, Spain*

[2]*Kamerlingh Onnes Laboratory, Leiden University, NL-2300 RA Leiden, The Netherlands*

[3]*ISIS Facility, Rutherford Appleton Laboratory, Chilton, Didcot OX11 0QX, United Kingdom*

[4]*Department Radiation, Radionuclides & Reactors, Section FAME, Delft University of Technology, NL-2629 JB Delft, The Netherlands*

[5]*Departamento de Física Aplicada I, Universidad de Málaga, E-29071 Málaga, Spain*

[6]*Institut für Chemie, Universität Osnabrück, Barbarastrasse 7, D-49076 Osnabrück, Germany*

[7]*Center for Radiation Detection Materials and Systems, Materials Science and Technology Division, Oak Ridge National Laboratory, Oak Ridge, Tennessee 37831-6056, USA*

Low-temperature magnetic susceptibility and heat-capacity measurements on nanoparticles ($d \approx 2.6$ nm) of the antiferromagnetic compounds DyPO$_4$ ($T_N = 3.4$ K) and GdPO$_4$ ($T_N = 0.77$ K) provide clear demonstrations of finite-size effects, which limit the divergence of the magnetic correlation lengths, thereby suppressing the bulk long-range magnetic ordering transitions. Instead, the incomplete antiferromagnetic order inside the particles leads to the formation of net magnetic moments on the particles. For the nanoparticles of Ising-type DyPO$_4$ superparamagnetic blocking is found in the ac susceptibility at $\simeq 1$ K, those of the XY-type GdPO$_4$ analog show a dipolar spin-glass transition at $\simeq 0.2$ K. Monte Carlo simulations for the magnetic heat capacities of both bulk and nanoparticle samples are in agreement with the experimental data. Strong size effects are also apparent in the Dy^{3+} and Gd^{3+} spin dynamics, which were studied by zero-field muon spin rotation (μSR) and high-field ^{31}P-nuclear magnetic resonance (^{31}P-NMR) nuclear relaxation measurements. The freezing transitions observed in the ac susceptibility of the nanoparticles also appear as peaks in the temperature dependence of the zero-field μSR rates, but at slightly higher temperatures, as to be expected from the higher frequency of the muon probe. For both bulk and nanoparticles of GdPO$_4$, the muon and ^{31}P-NMR rates are for $T \geqslant 5$ K dominated by exchange-narrowed hyperfine broadening arising from the electron spin-spin interactions inside the particles. The dipolar hyperfine interactions acting on the muons and the ^{31}P are, however, much reduced in the nanoparticles. For the DyPO$_4$ analogs the high-temperature rates appear to be fully determined by electron spin-lattice relaxation processes.

PACS number(s): 75.30.Gw, 75.40.Cx, 75.40.Mg, 75.50.Tt

I. INTRODUCTION

The last few years have witnessed a dramatically increased level of interest in quantum size effects in ligand-stabilized magnetic nanoparticles, notably the so-called single-molecule magnets, in which the nanoparticles carry large net magnetic moments due to the ferro- or ferrimagnetic spin arrangements inside the magnetic cores of the macromolecules. In contrast, size effects in nanosized particles of antiferromagnetic insulators with compensated sublattices (in bulk) have received much less attention, in spite of their potential fundamental importance.[1–4] In this paper, we present a study of the thermodynamic properties and spin dynamics of nanoparticles of two different types of 3D antiferromagnets, that is, the well-known anisotropic Ising antiferromagnet DyPO$_4$ and its more isotropic counterpart GdPO$_4$. In bulk DyPO$_4$ strong ligand field effects leave an effective spin $S = \frac{1}{2}$ Kramers doublet as the lowest-lying magnetic level, with highly anisotropic g tensor, $g_{\parallel} \simeq 19.5$ and $g_{\perp} \simeq 0$. A transition to long-range antiferromagnetic (AF) ordering occurs around $T_N = 3.4$ K.[5] For GdPO$_4$ recent heat capacity experiments evidenced a magnetic transition at $T_N = 0.77$ K.[6] Since, thus far, no detailed magnetic measurements appear to have been reported on this material, we have studied the magnetic behavior of a bulk-GdPO$_4$ single crystal by field-dependent ac-susceptibility measurements. Our data confirm that GdPO$_4$ has a transition

to an AF ordered state at $T_N = 0.77$ K and that below T_N it magnetically behaves as a compensated antiferromagnet with strong planar (XY-type) anisotropy induced by the combination of crystal-field effects and dipolar interactions.

The comparison of our susceptibility and magnetic heat-capacity data on the nanoparticles with the corresponding bulk quantities reveals interesting experimental examples of finite-size effects on the magnetic phase transitions, which had previously been mainly studied theoretically.[2] Monte Carlo (MC) simulations performed for either Ising spins or classical Heisenberg spins on the appropriate lattices are also reported, and they compare favorably with the experimental data for both the bulk and the nanoparticle samples. Pronounced size effects are likewise found in the phonon contributions to the heat capacity data, as measured from 10 K up to room temperature. Finally, effects of finite size on the spin dynamics were studied by means of ^{31}P-nuclear magnetic resonance (^{31}P-NMR) and μSR experiments. The analysis of the temperature dependence of the measured relaxation rates in the region of the magnetic ordering phenomena proved to be fully consistent with the results from the thermal and magnetic data. At more elevated temperatures, the rates appear to be determined by electron spin-spin fluctuations (of exchange and dipolar origin) for the GdPO$_4$ case and by various forms of electron spin-lattice relaxation for the DyPO$_4$ analogs.

II. EXPERIMENTAL DETAILS

Phosphates of the cerium group (RPO_4 with $R =$ La up to and including Gd) have a monoclinic monazite structure, whereas those of the yttrium group (RPO_4 with $R =$ Dy to Lu) have a tetragonal xenotime structure. The two structure types are closely related, such that the monazite structure can be viewed as a low-symmetry derivative of the zircon structure. Dy^{3+} is a magnetic rare-earth ion with an electronic configuration Xe $4f^9$. The ground-state multiplet is $^6H_{15/2}$, corresponding to $L = 5$ and $S = \frac{5}{2}$. In the $DyPO_4$ lattice, the multiplet becomes split into eight Kramers doublets by the crystal field of tetragonal symmetry.[5,7] Since the distance separating the lowest excited states from the ground doublet is about 100 K or higher, the low-temperature magnetic properties of the Dy^{3+} ion can be described in terms of an effective spin $S = \frac{1}{2}$ with a very anisotropic g tensor, that is, $g_\parallel = 19.5$ and $g_\perp = 0.5$. Neutron diffraction measurements[8] confirmed that $DyPO_4$ has the tetragonal zircon crystal structure, with linked DyO_4 and PO_4 tetrahedra sharing O atoms.[9] As opposed to Dy^{3+}, Gd^{3+} with the electronic configuration Xe $4f^7$, is a more isotropic magnetic rare-earth ion. Since its ground-state multiplet is $^8S_{7/2}$, corresponding to $S = \frac{7}{2}$ and $L = 0$, and thus no orbital moment, crystal field effects can only occur in higher order, by mixing excited states into the ground state. Bulk $GdPO_4$ belongs to the class of monazites, with a monoclinic unit cell, space group $P2_1/n$. There are four nonequivalent Gd^{3+} ions in the unit cell. Each Gd^{3+} ion is surrounded by six nearest-neighboring ions at distances varying between 4.0 and 4.2 Å.

Powder samples of $DyPO_4$ and $GdPO_4$ nanoparticles were prepared according to the methods described in Refs. 10 and 11. The nanoparticles are stabilized by nonmagnetic tris-(ethyl-hexyl)-phosphate ligand molecules, abbreviated TEHP $= (C_8H_{17}O)_3PO$. In our powder samples, the spherically shaped nanoparticles are densely packed in a random orientation. The narrow size distribution of the RPO_4 cluster cores was revealed by x-ray diffraction (XRD), tunneling electron microscopy (TEM), and small-angle x-ray scattering (SAXS) measurements. Dynamic light-scattering measurements show an overall particle size, that is, including the organic ligand shell, of about 3.5 nm. From the SAXS and TEM studies, the average size of the RPO_4 cores was found to be about 2.6 nm for both $DyPO_4$ and $GdPO_4$, corresponding to about 150 rare-earth ions per particle and a surface-to-volume ratio for the cores of about 2/3. In agreement with the TEM pictures, the x-ray-powder-diffraction patterns of the powder samples through the rare-earth series reveal a good crystallinity for the particles, in particular for the smaller-size (Ce to Sm) and larger-size (Er to Lu) rare-earth ions. These nanoparticles have an average size of 3 to 5 nm and are found to show exactly the same crystal structure as their bulk counterparts, that is, the monoclinic monazite structure from Ce up to Gd phosphate and the tetragonal xenotime from Dy up to Lu phosphate. In the bulk materials, the Tb phosphate (Tb being neighbored by Gd and Dy) is reported to be dimorphic. In the case of the nanoparticles, this separation line between the two phases is spread into an intermediate region stretching from Eu to Ho, that is, including the Gd and Dy phosphates that directly border the Tb phosphate. For these rare-earth ions the average

particle core size is found to be much smaller, about 2 nm, and the x-ray-powder-diffraction patterns appear to be appreciably broadened, exhibiting apparently a "mixed" crystal phase that shares the characters of both the monoclinic and tetragonal phases. Both features can be attributed to the smaller size of the particles in this intermediate lanthanide region, in combination with the near equivalency of the lattice energies for the two crystal phases in this region. The proximity in energy of the two phases and the large surface fraction likely entails a relatively large number of lattice defects that may lead to the occurrence of different crystallographic domains in the same particle core.

Magnetic (dc) data down to 2 K and in fields up to 5 T were obtained with a commercial SQUID magnetometer. The ac susceptibility in the range 50 mK $< T <$ 6 K was measured with a home-built mutual inductance susceptometer, mounted in a dilution refrigerator and operating at frequencies between 100 Hz and 7 kHz. Low-temperature heat capacity was measured in the same dilution refrigerator with a home-built calorimeter, using a thermal relaxation method. Additional heat capacity data up to room temperature were recorded in a commercial (Quantum Design MPMS) apparatus. The ^{31}P-nuclear magnetic resonance (^{31}P-NMR) studies ($I = \frac{1}{2}$, $\gamma/2\pi = 17.2333$ MHz/T) were performed by standard pulse NMR techniques in magnetic fields of $B_{app} = 9.4$ and 5.6 T. The μSR measurements were performed at ISIS (Rutherford Appleton Laboratory) on the MUSR beam line in zero field (ZF) and in a longitudinal field (LF), using a statistics of about 20×10^6 events.

III. MAGNETIC MEASUREMENTS

Figure 1 shows the temperature dependence of the molar susceptibility χ_{nano} of the nanoparticles for both $DyPO_4$ (from Ref. 12) and $GdPO_4$, as measured by SQUID magnetometry down to 2 K and complemented by ac-susceptibility measurements to lower temperatures. The ac and dc data showed perfect overlap in the range 2 K–5 K in all cases. For comparison, relevant susceptibility data for the bulk counterparts are included. For $GdPO_4$ the bulk is represented by the average of the susceptibility measured for the different crystallographic directions, noting that the susceptibility already becomes independent of orientation above $T \approx 1.2 \times T_N$ (see Appendix). For $DyPO_4$, we compare with the published[5] parallel susceptibility $\chi_\parallel$ of the bulk, the susceptibility in the perpendicular directions being negligibly small due to the strong uniaxial g anisotropy. As seen in Fig. 1, in the region near to and below the bulk magnetic ordering temperatures, the susceptibility, χ_{nano}, of the nanoparticles becomes strongly different from the bulk behaviors. In both cases, apart from a slight discontinuity, not visible on the scale of Fig. 1, no sign of the bulk AF ordering phenomenon is discernible in χ_{nano} at temperatures corresponding to the bulk T_N. Instead, frequency-dependent cusps appear in χ_{nano} at lower temperatures, that is, around 0.2 K and 1 K for $GdPO_4$ and $DyPO_4$, respectively. In Fig. 2, we report the frequency-dependent ac-susceptibility measurements of these cusps. We note further that in the paramagnetic range, that is, far above the bulk T_N, the curves for χ_{nano} and χ_{bulk} are found to have the same temperature dependence and can thus be directly scaled upon one another, which is, in fact, to be expected. For isotropic $GdPO_4$ this
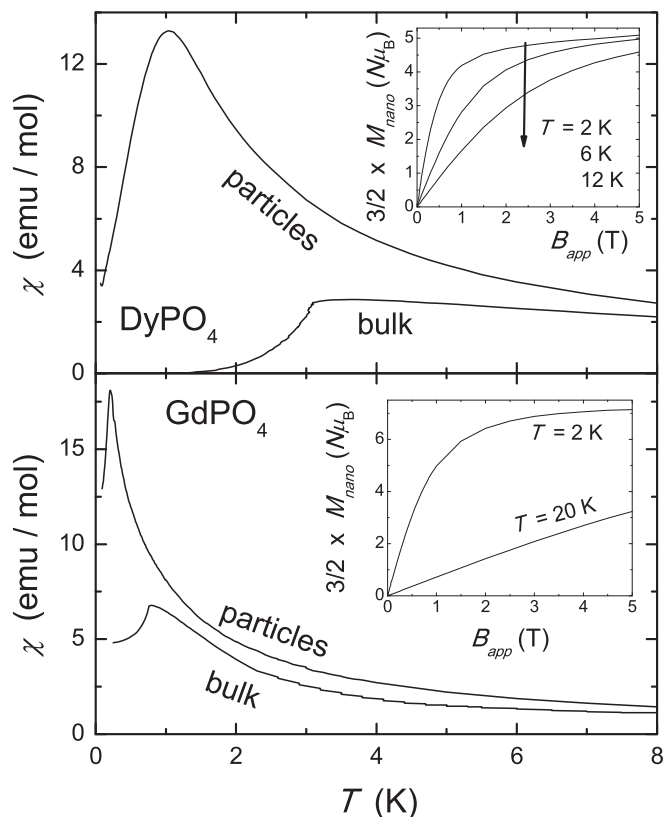
FIG. 1. Low-field susceptibility $\chi(T)$ and measured (reversible) magnetization curves (insets) of the $DyPO_4$ (top) and $GdPO_4$ (bottom) nanoparticles. The parallel susceptibility ($\chi_\parallel$) of bulk $DyPO_4$ (from Ref. [5]) and the powder susceptibility measured for bulk $GdPO_4$ are included for comparison.
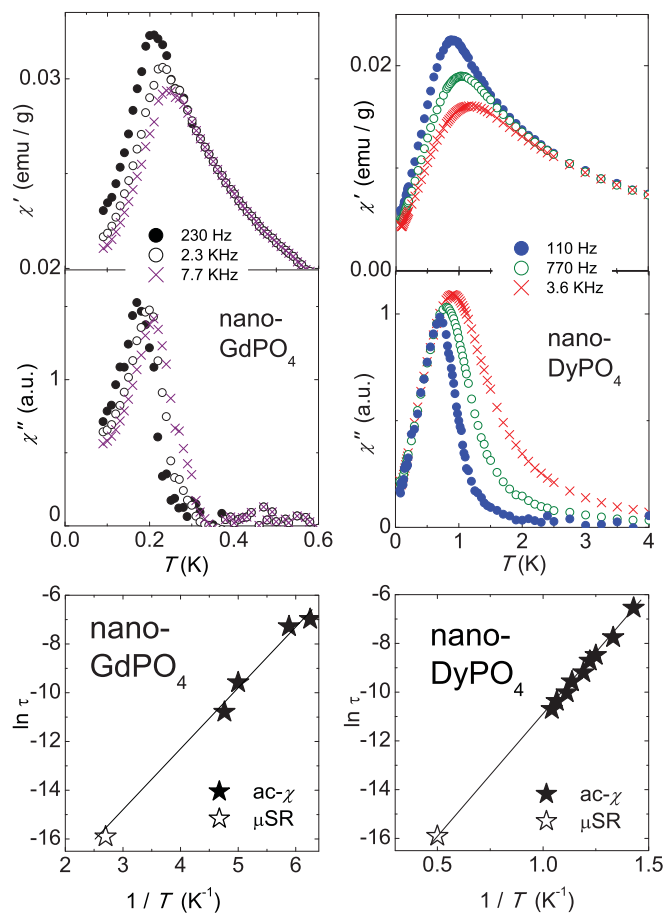

FIG. 2. (Color online) Frequency dependence of the ac susceptibility measured for the $GdPO_4$ (left) and $DyPO_4$ (right) nanoparticles in the region near to the cusps. In the lowest frames, the frequency dependence of the temperatures of the maxima is analyzed in terms of the Arrhenius law. An additional data point determined from μSR experiments (see Sec. VI) is included for both.

is self-evident; the only scaling factor between the powder susceptibilities being the mass ratio between the RPO_4 cores and the ligands in the nanoparticle sample. For $DyPO_4$, the powder χ_{nano} is compared to the bulk $\chi_\parallel$ so an additional scaling factor of $1/\sqrt{3}$ arises since, with $g_\perp \simeq 0$, the effective g value for the nanoparticle powder becomes $g_\parallel/\sqrt{3}$. Since the mass fraction of the RPO_4 cores in the ligand-capped nanoparticles could only approximately be determined from the chemical syntheses, more accurate values were obtained from this direct scaling of χ_{nano} to χ_{bulk} at high temperatures, yielding an RPO_4 fraction of about 2/3 in both cases indeed. The same value for the mass fraction was further deduced from the scaling of the measured saturation molar magnetization values at the lowest temperature (see insets of Fig. 1) to the expected bulk powder values, that is, $\approx 5.1 N\mu_B$ for $DyPO_4$ and $7 N\mu_B$ for $GdPO_4$.

The strongly different behavior of χ_{nano} as compared to χ_{bulk} in the low-T range can be fully understood in terms of finite-size effects. First, since the increase of the magnetic correlation length as $T \to T_N$ is limited by the particle size, the phase transition to long-range AF order becomes suppressed.[2] Second, missing magnetic neighbors at the particle surfaces will lead to net magnetic moments μ per particle due to incomplete compensation of the AF sublattices and, thus, to a superparamagnetic signal superposed upon the AF background susceptibility.[3] To obtain an estimate of μ, we subtracted the

bulk susceptibilities from the (scaled) χ_{nano} curves and fitted the remaining signals to the Curie-Weiss law. From the so-obtained Curie constants, the average number of unpaired spins per particle can be estimated. For the $DyPO_4$ nanoparticles, this number is found to be as high as $\approx 20\%$. Since the mean particle core diameter is 2.6 nm,[11] implying ≈ 150 Dy^{3+} spins per particle, one-third of which will be in the inner core and, thus, fully AF coordinated, this fraction would then correspond to ≈ 30 uncompensated spins and ≈ 70 compensated spins in the surface layer of the $DyPO_4$ particle cores. For the $GdPO_4$ nanoparticles, on the other hand, we find $\mu \approx 80\mu_B$, corresponding to about 11 uncompensated Gd^{3+} ($S = \frac{7}{2}$) spins per particle only. The effective number of uncompensated spins in the surface layer is, therefore, only about 10% as compared to 30% for the $DyPO_4$ analog. Since in both cases the number of surface spins with missing magnetic neighbors will be similar, we attribute the difference to the more isotropic nature of the AF interaction between the Gd^{3+} spins, as opposed to the strongly anisotropic Ising interaction in $DyPO_4$. The lower the anisotropy of the interaction, the easier it will be for the spins inside a finite volume to arrange themselves in such a

configuration that the resulting net moment of the particle will be a minimum.

Furthermore, the properties of the superparamagnetic contributions associated with the net moments per particle will also depend strongly on the type and strength of the anisotropy. For the highly anisotropic Ising system DyPO$_4$, the origin of the observed cusp in χ_{nano} can be attributed to the well-known phenomenon of superparamagnetic blocking, occurring when the thermal energy becomes less than the anisotropy barrier E_A opposing inversion of the net particle moment (μ). From the value of the freezing (blocking) temperature, $T_f \approx 1$ K, E_A can be estimated as ≈ 10 K. Analyzing the frequency dependence observed for the cusp in χ_{ac}, as shown in Fig. 2, in terms of a simple Arrhenius law with relaxation time $\tau = \tau_0 \exp(E_A/k_B T)$, yields the same value for $E_A = (10.5 \pm 0.3)$ K indeed, with $\tau_0 \approx 4 \times 10^{-10}$ s. Interestingly, the plot can be extended to much higher frequency (MHz range) since, as is shown below, the blocking phenomenon is likewise observed in the μSR data, giving the additional data point in this plot.

For the magnetically more isotropic GdPO$_4$ nanoparticles, the cusp in χ_{nano} is observed at much lower temperature, that is, ≈ 0.2 K, and the dependence on the ac frequency of the temperature of the susceptibility maximum is much less pronounced (see Fig. 2). Thus, although we attribute the cusps in both cases to "freezing" of the net particle moments μ at low-enough temperature, in the case of DyPO$_4$ the freezing arises primarily from the Ising-type anisotropy of the particles, that is, from superparamagnetic blocking, whereas for GdPO$_4$ it is ascribed to the dipolar interactions between the net particle moments. Since the particles are closely packed in a random array, these interactions result in a dipolar spin glass. Indeed, when using the value for $\mu \approx 80\mu_B$ determined from χ_{nano} for GdPO$_4$ and the estimated distance $r \approx 6$ nm between two neighboring particle moments, the estimated dipolar energy μ^2/r^3 just equals the thermal energy $k_B T_{\text{max}}$ corresponding to the observed $T_f \approx 0.2$ K. Furthermore, a major difference to be noted from Fig. 2 is that the χ_{nano} for GdPO$_4$ extrapolates to a large finite value for $T \rightarrow 0$, as expected for an (isotropic) spin glass,[13] whereas it extrapolates to zero for the DyPO$_4$ case, in agreement with superparamagnetic blocking. Last, when characterizing the frequency dependence of the freezing temperatures by the derivative $\Delta T_f / (T_f \Delta \log f)$, we obtain a value of 0.08 for this quantity for the case of GdPO$_4$, as compared to 0.18 for the DyPO$_4$ analog. The small value found for GdPO$_4$ is, indeed, typical for spin glasses, whereas that for DyPO$_4$ is comparable to those reported for superparamagnetic blocking.[13] As shown in Fig. 2 (bottom), the frequency dependence of the cusp in χ_{ac} can be nicely fitted to the Arrhenius law, in this case with relaxation time $\tau_0 \approx 5.6 \times 10^{-10}$ s and activation energy $E_A = 2.3$ K. Similarly to that seen with the DyPO$_4$ nanoparticles, also in this case, an additional data point in the MHz range in this plot is provided by the μSR data discussed below, in which the freezing phenomenon is likewise observed.

IV. HEAT-CAPACITY MEASUREMENTS

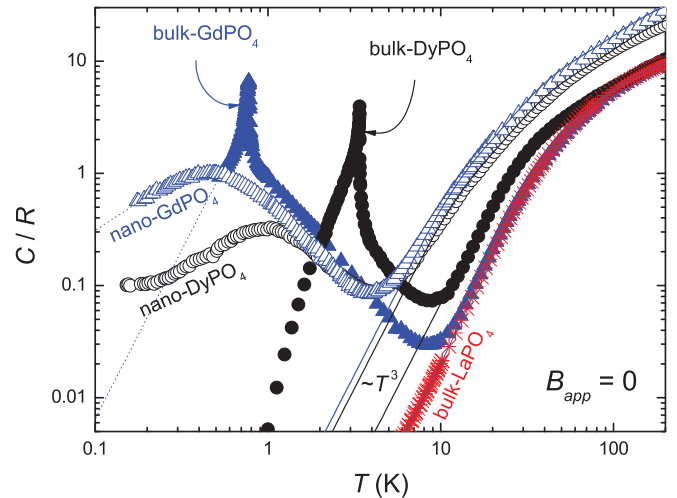Figure 3 shows our measurements of the ZF heat capacity C/R of the nanoparticles, together with data for their bulk

FIG. 3. (Color online) Temperature dependence of the ZF heat capacity for GdPO$_4$ and DyPO$_4$ nanoparticles and their bulk counterparts. Data for nonmagnetic bulk LaPO$_4$ are included. The solid curves are the estimated lattice contributions. We note that the molar heat capacity values displayed here were calculated on the basis of the RPO$_4$ molecular weights for both bulk and nanoparticle samples (compare with Fig. 6).

counterparts and for nonmagnetic LaPO$_4$. Data for bulk DyPO$_4$ were taken from the paper by Wright *et al.*[5] (up to 4 K) complemented by our own results taken in the range 4 K–300 K. Data for bulk GdPO$_4$ and LaPO$_4$ were taken from the paper by Thiriet *et al.*[6] The magnetic heat capacities in Fig. 3 are seen to be superposed on the lattice phonon contribution C_{ph}, which for bulk monazites, is expected to be given to a high approximation by the data for the nonmagnetic LaPO$_4$ isomorph. Indeed, for $T \geqslant 15$ K, the data for GdPO$_4$ and LaPO$_4$ are seen to nicely coincide. As shown by the solid curve drawn through these data, they can be well fitted by a simple Debye model, following the well-known T^3 approximation up to ≈ 20 K with a calculated Debye temperature $\Theta_D = 227$ K. The lattice heat capacity of the bulk DyPO$_4$ compound, having the tetragonal zircon lattice, is seen to lie substantially above that of the monazites from 10 K up to about 70 K, after which it converges to the same high-temperature limit. At the highest temperatures, the three bulk heat capacities all appear to extrapolate to the value of 18 R, which would be in agreement with the classical Dulong and Petit law, predicting a contribution of 3 R for every degree of freedom (per atom in the chemical formula). The value estimated for the Debye temperature for DyPO$_4$ is $\Theta_D \simeq 150$ K, much lower indeed than that found for the La and Gd monazites. This indicates the tetragonal DyPO$_4$ lattice to be "softer" than the monoclinic sister compounds, in agreement with the larger size of its unit cell.[11] For the nanoparticles, we observe quite similar phonon contributions above 10 K for both Dy and Gd. The phonon contributions are, thus, much higher than for the bulk materials, which can be attributed principally to the extra vibrational contributions coming from the TEHP ligand molecules, as is further discussed below.

We first concentrate on the magnetic heat-capacity contributions obtained by subtraction of the phonon portions approximated by the T^3 temperature dependencies, as indi-
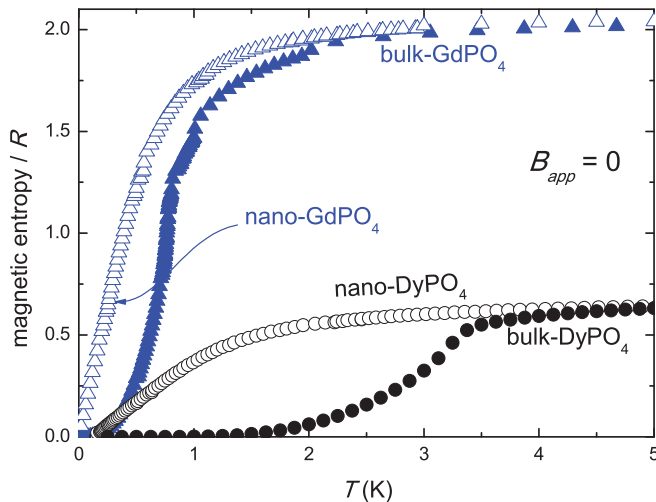
FIG. 4. (Color online) Magnetic entropies obtained by integration of the (zero-field) magnetic heat capacity contributions for the different samples, as indicated.

FIG. 5. (Color online) Temperature dependence of the magnetic heat capacity for the DyPO$_4$ nanoparticles in applied fields ($B_{app} = 0, 1$ T, and 3 T). Solid curves, calculated Zeeman-split contributions (adding $B_{int} = 0.27$ T to B_{app}; see text); dotted curve, estimated nuclear heat capacity C_{hf}.

cated by the solid lines in Fig. 3. For the bulk samples, the magnetic heat capacities clearly show the pronounced λ-type anomalies at $T_N = 0.77$ K and 3.4 K for GdPO$_4$ and DyPO$_4$, respectively, associated with the transitions to long-range magnetic order. As mentioned above for the nanoparticles, the finite particle size sets a limit on the magnetic correlation length and, thereby, prohibits the development of a long-range magnetically ordered state. Accordingly, instead of the λ-type bulk heat capacity peaks, broad anomalies are found at lower temperatures, reflecting the development of short-range AF correlations inside the nanoparticles. The temperatures of these maxima, about 0.4 K and 1.0 K, respectively, are close to the respective freezing temperatures found in the susceptibility, which is consistent, since the occurrence of freezing of the (net) particle moments obviously necessitates the presence of well-developed *intra* particle magnetic correlations as a precursor.

By subtracting the lattice phonon contributions C_{ph} as described from the raw data, the magnetic heat capacity contributions C_m are obtained. Thus, by taking the integral $\int (C_m/T)\mathrm{d}T$, the magnetic entropies involved in the ordering processes can be calculated (see Fig. 4). To enable the integration for bulk GdPO$_4$, the data below 0.5 K in Fig. 3 were extrapolated by a T^3 dependence, expected from spin-wave theory for the three-dimensional Heisenberg antiferromagnet. At high temperatures, the magnetic heat capacities for all samples can be well approximated by a T^{-2} dependence, that is, the high-temperature limiting behavior common to all magnetic substances. After scaling the magnetic heat capacities of the nanoparticles with the factor of 2/3 obtained in the above for the mass fractions of RPO_4 in the samples, these estimates lead in *all four* cases to the correct values of $R \ln(2S + 1)$ expected for the total magnetic ordering entropies, that is, the value $R \ln(2)$ for nano- and bulk DyPO$_4$ (with spin $S = \frac{1}{2}$) and $R \ln(8)$ for the Gd counterparts ($S = \frac{7}{2}$).

In addition to these ZF measurements, field-dependent heat-capacity measurements were made on the DyPO$_4$ nanoparticles, as displayed in Fig. 5. As before, the magnetic
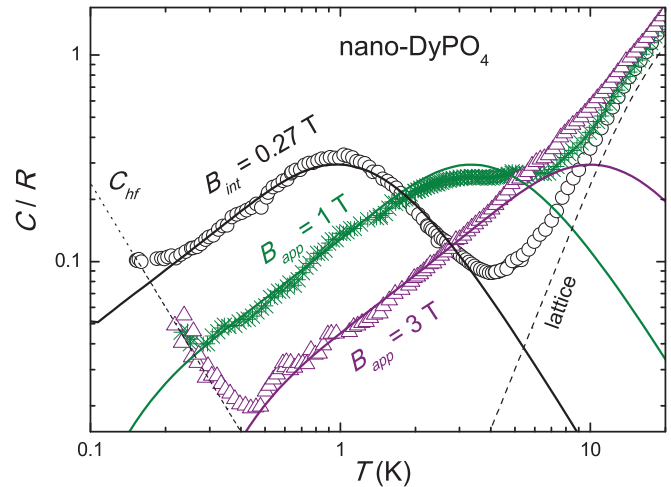
contributions are obtained by subtracting the lattice term indicated in the figure. The thus-obtained Schottky-type heat capacity anomalies were analyzed in the following way: in a mean-field approach, the onset of intraparticle magnetic correlations can be interpreted in terms of an interaction field B_{int}, producing a Zeeman splitting of the (otherwise degenerate) Dy^{3+} ground doublet and, thus, leading to a Schottky-type anomaly, as observed. As is further discussed in the following section, the interaction field B_{int} stands for the combination of the magnetic exchange and magnetic dipolar interactions; that is, it is the sum of the exchange and dipolar fields. When measuring $C(T)$ in applied field B_{app}, the total field becomes the sum of B_{int} and B_{app}, so the anomaly should shift toward higher temperature with increasing B_{app}. This effect is indeed observed in Fig. 5, which shows $C_m(T)$ of the nanoparticles for $B_{app} = 0$ together with data measured for $B_{app} = 1$ T and 3 T. We calculated $C_m(T)$ arising from the Zeeman-split ground doublet by considering averages over random orientations of the particles' anisotropy axes with respect to B_{app}. To analyze the $C_m(T)$ for $B_{app} = 0$, the splitting of the Dy^{3+} doublets due to B_{int} was introduced as a free parameter. As shown in Fig. 5, an excellent description of the $B_{app} = 0$ curve is obtained for $B_{int} = 0.27$ T. For $B_{app} = 1$ T and 3 T, we add B_{int} to B_{app}, obtaining the solid lines in Fig. 5, which nicely reproduce the data except at lowest temperatures, where one notices an upward curvature following the law $CT^2/R \simeq 2.4 \times 10^{-3}$ K^2 (dotted curve). Since this term, C_{hf}, is independent of B_{app}, it is ascribed to the hyperfine splitting (*hf*) of the magnetic levels of the Dy nuclei (the associated hyperfine fields B_{hf} are much larger than B_{app}). The dotted line represents C_{hf} as calculated with hyperfine constants $A_{hf} = 65$ mK and $A_{hf} = 92$ mK for the ^{161}Dy and ^{163}Dy isotopes, respectively. These values are close to those reported by Cooke and Park[14] and correspond to $B_{hf} \approx 24$T $\gg B_{app}$. The value found for B_{int} is, however, a factor of three smaller than the $B_{int} = 0.78$ T known for bulk DyPO$_4$.[5] The much smaller value should be due to the fact that a substantial

fraction of the surface spins are not fully antiferromagnetically coordinated in the DyPO$_4$ clusters, in combination with a decrease of the magnetic interactions due to lattice expansion and/or lattice defects as seen in the XRD patterns. Also, the dipolar contribution to the magnetic interaction, which in bulk DyPO$_4$ is comparable to the exchange part, can be expected to be reduced in the nanoparticles. The MC simulations discussed in the next section are found to agree with these qualitative arguments.

Besides the integral $\int (C_m/T)dT$, giving the magnetic entropy, the integral of the magnetic heat capacity curve itself, that is, $\int C_m dT$, should be equal to the total magnetic energy, $E_m = E_{ex} + E_{cf} + E_{dip}$, involved in the magnetic ordering process. Here the three terms on the right-hand side stand for the magnetic exchange, the crystal-field interaction and the dipolar interaction energies, respectively. Neglecting zero-point corrections to the AF ground state, the full expression for the energy per spin, E_m/N, can be written as

$$E_m/N = z|J|S^2 + (1/3)|D|S(2S-1) + (1/2)g\mu_B S B_{dip},$$

where z is the number of nearest magnetic neighbors and a crystal-field interaction of uniaxial symmetry is assumed, that is, a term $-DS_\alpha^2$ in the Hamiltonian. B_{dip} stands for the dipolar field acting on a given spin due to the other moments in the crystal. Furthermore, these same parameters J, D, and B_{dip} enter in the expression for the coefficient of the limiting high-temperature T^{-2} term of the magnetic heat capacity, for which theory[15] predicts

$$CT^2/R = 2nz[S(S+1)|J|/3k_B]^2 + D^2 S(S+1)(2S-1)$$
$$\times (2S+3)/10k_B^2 + g^2\mu_B^2 S(S+1)B_{dip}^2/3k_B^2.$$

Here the numerical factor n in the exchange term should be taken as $n = 1$, 2, and 3 for Ising, XY, and Heisenberg type of magnetic interaction. Since the magnetic studies on bulk GdPO$_4$ presented in the Appendix evidence a large planar anisotropy (large compared to the exchange), we shall use the value $n = 2$ in the above formula. Furthermore, the exchange constant estimated from these data is $zJ/k_B = -0.080$ K, in good agreement with the value found from the MC simulations (see Sec. V), which yield the effective values $z\tilde{J}/k_B = -0.084$ K and $z\tilde{J}/k_B = -0.047$ K for bulk and nanosample of GdPO$_4$, respectively. The reduction by a factor of two of the (average) exchange interaction in the nanosample arises in the simulations from the missing magnetic neighbors near the surface of the particles and from the introduction of an average expansion by about 5% of the unit cell parameters, assuming a 12th power dependence of the exchange interaction on the interionic distances. The same MC simulations give the values $B_{dip} = 0.36$ T and $D/k_B = 0.08$ K for bulk GdPO$_4$, on the basis of which we calculate the total magnetic energy as $E_m = E_{ex} + E_{cf} + E_{dip} \simeq 1.0 + 0.6 + 0.8 = 2.4$ K, which compares favorably with the experimental value $E_m \simeq 2.2$ K obtained from the integration of the heat-capacity curve. In the case of the GdPO$_4$ nanoparticles, the experimental E_m amounts to ~1.4 K. Assuming the same anisotropy value for bulk and nanosamples, and adopting the value for the effective exchange $z\tilde{J}/k_B = -0.047$ K mentioned above, we calculate $E_{dip} = E_m - E_{ex} - E_{cf} \simeq 1.4 - 0.6 - 0.6 = 0.2$ K, from which we obtain $B_{dip} \simeq 0.1$ T, in fair agreement with the

dipolar field calculated in the MC simulations (see below). For the coefficient of the T^{-2} term, the resulting sum of exchange, dipolar, and crystal-field contributions amounts, therefore, to $0.1 + 0.6 + 1.2 = 1.9$ K^2 for the bulk sample and $0.04 + 0.60 + 0.08 = 0.72$ K^2 for the nanoparticles, to be compared with the experimental results of ~1.1 K^2 and ~0.6 K^2, respectively. Although the quantitative agreement is less perfect in this case, the strong differences in the values obtained for bulk and nanoparticle samples are again well accounted for.

For DyPO$_4$, the crystal-field term in the above equations is not present since it vanishes for (a Kramers doublet with effective) spin $S = \frac{1}{2}$. For bulk DyPO$_4$, the values of the AF exchange constant and the dipolar interactions have been well established in the literature.[5] This compound is particular since it was found that, although the long-range dipolar interactions are comparable in strength to the (short-range) superexchange interactions, the material is nevertheless a good approximation of an Ising system with only interactions between nearest neighbors. This arises because exchange and dipolar interactions from further-than-nearest neighbors almost completely cancel one another, their sum amounting to a mere 3% of the interaction between nearest neighbors. The dipolar and exchange contributions to the latter are in the ratio 40/60, and their sum can be represented to good approximation by an "effective" nearest-neighbor "exchange" interaction, $J/k_B = -2.50$ K. This is, indeed, confirmed by the MC simulations discussed below. In this approximation, therefore, one simply obtains $E_m = E_{ex} = z|J|S^2 = 2.50$ K for the total magnetic energy of the bulk sample. Alternatively, in terms of a nearest-neighbor (nn) exchange interaction in combination with the (total) dipolar interaction, the magnetic properties are found to be well described by a nn exchange $J/k_B = -1.80$ K, corresponding to an exchange field $B_{ex} = 0.550$ T in the mean-field formalism, plus a dipolar field $B_{dip} = 0.237$ T. The formula for the magnetic energy then becomes $E_m = E_{ex} + E_{dip} \simeq 1.80 + 0.79 = 2.59$ K. For the nanosample, the MC simulations again point to a strong reduction of the average magnetic interactions that can be described in terms of a unit cell expansion of 7%, leading to $\tilde{J}/k_B = -0.44$ K and dipolar field $B_{dip} = 0.116$ T. The resulting total interaction field B_{int} is, thus, 0.252 T as compared to 0.787 T for the bulk case, confirming the substantial reduction of B_{int} in the nanoparticles found in the analysis of the field-dependent heat capacity measurements, which yielded the estimate $B_{int} = 0.27$ T. For the nanosample the prediction for the magnetic energy, therefore, becomes $E_m = E_{ex} + E_{dip} \simeq 0.44 + 0.38 = 0.82$ K. Experimentally, the areas under the heat-capacity curves yield total energies $E_m \simeq 2.38$ K and 0.95 K for bulk and nanosample, in good agreement, given the experimental uncertainties and averages over particles involved. The same reduction can be seen in the experimental coefficient of the T^{-2} term, which experimentally for the DyPO$_4$ nanoparticles, is indeed a factor of four to five smaller than for the bulk, namely, $CT^2/R = 0.7$ K^2 versus 3.3 K^2 (see Fig. 3). From the above theoretical expression for the coefficient of the experimental T^{-2} term, now with the Ising value $n = 1$, the calculated values for the bulk sample are 3.1 K^2 and 4.0 K^2, depending on whether the single effective nn interaction or the combination

of nn exchange plus dipolar interaction is used. For the nanosample the mentioned values for $\tilde{J}/k_B$ and B_{dip} yield the value 0.67 K^2. The agreement with experiment is again satisfactory for both samples.

We conclude this section with a discussion of the phonon heat-capacity contributions in the two nanosamples. These are obtained by subtracting from the heat capacity per gram of sample, C_g^{nano}, as measured in the range $T > 5$ K, the magnetic contributions (likewise per gram) discussed above, namely, the associated high-temperature T^{-2} tails of the broad magnetic anomalies. As an approximation, we may consider in the analysis the RPO$_4$ cores of the particles as being embedded in a softer medium formed by the TEHP-ligand "shells" that surround these cores. Such an approach has been successfully applied previously in studies of the (structurally similar) molecular metal cluster compounds, namely, for the analysis of the heat-capacity measurements and the Mössbauer recoilless fractions (Debye-Waller factors).[16,17] The lattice vibrations are then divided in two different classes, the (high-energy/small-wavelength) intracluster vibrations of the atoms in the much stiffer particle cores and the (low-energy/long-wavelength) intercluster vibrations corresponding to the center-of-mass motions of the cores in the surrounding medium. In the analysis, the two types of vibrations are taken to be decoupled, an assumption that is justified *a posteriori* by the fact that the associated intra- and intercluster Debye temperatures are found to differ by an order of magnitude, with $\Theta_D^{\text{inter}} \ll \Theta_D^{\text{intra}}$. It is of interest to note that the measured low-temperature heat capacities of molecular magnetic cluster compounds can indeed be likewise described by a large fraction of low-energy excitations, with Debye temperatures of the order of 10 K–30 K.[18]

Proceeding along these lines and taking into account the RPO$_4$ mass fraction of about 2/3 found in the above from the magnetic data, we consider the contributions to C_g^{nano} from RPO$_4$ cores and ligands to be additive and write

$$C_g^{\text{nano}} = \tfrac{2}{3}C_g^{\text{REPO}_4} + \tfrac{1}{3}C_g^{\text{ligand}}.$$

In order to obtain an estimate of C_g^{ligand}, we further assume the phonon contributions from the RPO$_4$ cores to be the same as those of their bulk counterparts. Although this may certainly be questioned, the error involved will be small since the RPO$_4$ contributions are, at any rate, much smaller than the ligand part. This can already be directly inferred from Fig. 3 from the fact that above 5 K the lattice heat capacities of the nanoparticles lie far above the bulk data and are almost equal in spite of the fact that the bulk data are much larger for $R = \text{Dy}^{3+}$ than for $R = \text{Gd}^{3+}$, and the volume ratio of the Dy and Gd nanoparticles is of the order of $(3.5/2.6)^3 = 2.4$. A large ligand contribution is also expected on theoretical grounds since the number of vibrational degrees of freedom (i.e., the number of atoms per chemical formula unit) of the TEHP $= (\text{C}_8\text{H}_{17})_3\text{PO}_4$ molecules is evidently much larger than that of the RPO$_4$. Thus the expected high-temperature Du Long and Petit limit for the molar heat capacity of TEHP is 240 R as compared to 18 R for RPO$_4$. The thus-derived estimates of C_g^{ligand} for the two samples are plotted in Fig. 6 and fitted to the Debye function, giving a Debye temperature of $\Theta_D^{\text{inter}} \simeq 55$ K, much lower indeed than the above-obtained
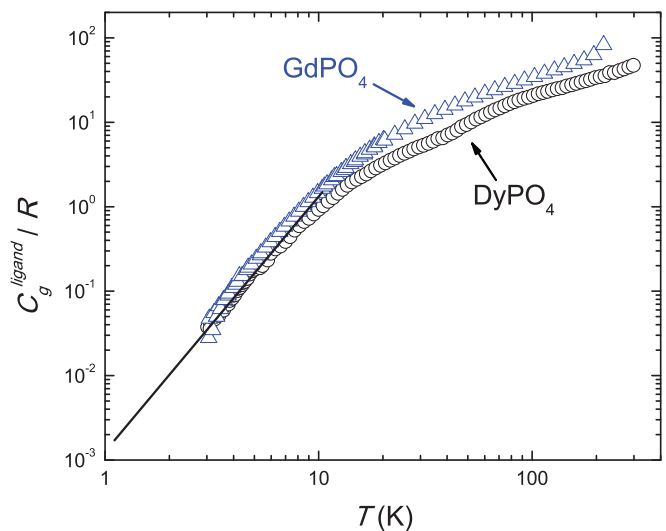

FIG. 6. (Color online) Temperature dependence of the estimated lattice heat capacity contributions from the TEHP ligands (C_g^{nano}). The solid curve shows the fitted Debye function with $\Theta_D^{\text{inter}} \simeq 55$ K. We note that the values for the molar heat capacity in this figure were calculated using the molecular weight of the TEHP ligand (compare with Fig. 3).

values for the bulk RPO$_4$ compounds. Dividing by the molecular weight of the TEHP ligand yields the molar ligand heat capacity, C^{ligand}/R, as given by the vertical scale of Fig. 6. The thus-obtained two estimates for the ligand heat capacity appear to be in reasonable agreement, given all the uncertainties involved. It may be observed that the molar heat capacity at high temperatures tends, in fact, to values of the order of 100 R, in agreement with the Du Long and Petit prediction.

V. MONTE CARLO SIMULATIONS

For further analysis of the experimentally observed finite-size effects, we have performed MC simulations for the ZF heat capacity for bulk systems and nanoparticles made of crystallites of DyPO$_4$ and GdPO$_4$. We consider crystals of magnetic moments $g\mu_B\mathbf{S_i}$, where $\mathbf{S_i}$ are classical spins of modulus S placed on the N sites i of the crystal lattices. The Hamiltonian used reads

$$\mathcal{H} = -J\sum_{i,j}^{nn}\sum_{\alpha}S_i^{\alpha}S_j^{\alpha} - \frac{1}{2}\sum_{i,\alpha}\left(g\mu_B S_i^{\alpha}\right)B_{i,\text{dip}}^{\alpha} - \sum_i D\left(S_i^y\right)^2,$$

$$(5.1)$$

where the first sum is over Nz nn pairs (z is the number of nearest magnetic neighbors). Note that (i,j) and (j,i) appear as different pairs in the summation, J stands for the exchange energy, D for the uniaxial anisotropy, and $B_{i,\text{dip}}^{\alpha}$ for the α component ($\alpha = x, y, z$) of the dipolar field $\mathbf{B}_{\text{dip}}$ at site i:

$$B_{i,\text{dip}}^{\alpha} = \frac{\mu_0}{4\pi}g\mu_B\sum_{j,\beta}r_{ij}^3\left(\delta_{\alpha\beta} - 3r_{ij}^{\alpha}r_{ij}^{\beta}r_{ij}^{-2}\right)S_j^{\beta}. \quad (5.2)$$

Within the effective field formalism Eq. (5.1) can be rewritten as follows:

$$\mathcal{H} = -\frac{1}{2}\sum_{i,\alpha}\left(g\mu_B S_i^\alpha\right)B_{i,\text{ex}}^\alpha - \frac{1}{2}\sum_{i,\alpha}\left(g\mu_B S_i^\alpha\right)B_{i,\text{dip}}^\alpha$$
$$-\frac{1}{2}\sum_i(g\mu_B S_i^y)B_{i,\text{an}}^y, \qquad (5.3)$$

where

$$B_{i,\text{ex}}^\alpha = (2J/g\mu_B)\sum_{j=1}^{z}S_j^\alpha \quad \text{and} \quad B_{i,\text{an}}^y = (2D/g\mu_B)S_i^y$$

represent the local exchange and anisotropy fields, respectively, acting on the components ($\alpha = x, y, z$) of a reference spin S_i.

For DyPO$_4$, in its low-temperature pure Ising state, only a single spin component remains, say $\alpha = z$, so that $B_{\text{ex}} = 2zJS/g\mu_B$ for bulk systems. Since the crystal-field effects leave an effective spin $S = \frac{1}{2}$ as the only populated doublet, the anisotropy term [the third term on the right-hand side of Eq. (5.1)] is not relevant in this case. In order to compare the MC simulations with the experimental results for the nanoparticles, we find it useful to define

$$\tilde{z} = \sum_{j=1}^{z}S_j^\alpha/S.$$

Note that $\tilde{z}$, when averaged over ensembles of nanoparticles, may not coincide with z. We define an effective exchange constant as $\tilde{J} = \tilde{z}J/z$. In general, $|\tilde{J}| < |J|$ given that $\tilde{J}$ includes the effect of missing bonds and defects on the surface of the nanoparticles. The effective field B_{ex} and $\tilde{J}$ are directly related by $B_{\text{ex}} = 2z\tilde{J}S/g\mu_B$. In a similar way as in Sec. IV, the exchange energy per spin can be written as $E_{\text{ex}}/N = z|\tilde{J}|S^2$.

The dipolar interaction terms are included in Eq. (5.1) since the associated interaction energies between pairs of nn magnetic moments are on the order of 0.5 K and 1 K for GdPO$_4$ and DyPO$_4$, respectively, that is, comparable to the thermal energies $k_B T_N$ associated with the magnetic transition temperatures observed for the bulk compounds. In fact, for bulk DyPO$_4$, it has been reported[5,19] that the dipolar and exchange contributions to the magnetic interaction between nearest neighbors are in the ratio 40/60. The material is rather unique in that it is a good example of a magnetic compound with nearest-neighbor-only magnetic interactions, in spite of the fact that the long-range dipolar interactions play such an important role. The explanation is that the dipolar and exchange contributions with further (than nn) neighbors are again similar in magnitude, but of different sign. As a result, they almost fully cancel one another, leaving a net interaction with further neighbors that amounts to only about 3% of the nn interaction.[5,19]

In the calculations for DyPO$_4$, a tetragonal zircon lattice has been taken with $a = b = 6.917$ Å, $c = 6.053$ Å, and four Dy^{3+} ions per unit cell. Each Dy^{3+} has four equivalent magnetic nn at a distance 3.78 Å. We use a Cartesian system of axes, with the c axis coinciding with the z direction. The Dy^{3+} magnetic moments are represented by classical Ising spins, oriented along z, that can take values $S_i^z = \pm\frac{1}{2}$, with $g = 19.5$. For GdPO$_4$ we adopt the reported monoclinic

monazite structure, with four Gd^{3+} per unit cell and axes $a = 6.643$ Å, $b = 6.841$ Å, $c = 6.328$ Å. In our Cartesian system of axes, we take a and b to coincide with the x and z axes, respectively; the y axis, denoted by c' in the Appendix, is then nearly coincident with the crystallographic c axis (at an angle of about 14°). Each Gd^{3+} has six magnetic nn at distances lying in the interval [4.00 Å, 4.22 Å]. We treat the Gd^{3+} magnetic moments as classical three-dimensional spin vectors, with $S = \frac{7}{2}$ ($g = 2$) and the restriction that S_i^z can take only values $(-7/2, -5/2, \ldots, +7/2)$, with arbitrary azimuthal angles around the $z = b$ axis. Here we are predicating on the analysis of the field-dependent measurements of the differential susceptibility in the region of magnetic order, as discussed below in the Appendix. These data evidence a strong preference for the moments to lie within the ab (xz) plane, with the b axis as the most preferred direction in this easy plane.

For the bulk samples, we simulate systems of $16 \times 16 \times 16$ unit cells and use periodic boundary conditions. For the nanoparticles, we simulate spherical crystallites of diameter $d = 2.6$ nm, assuming the same lattice structure as for the bulk systems. The results are averaged over some hundreds of spheres, centered at different positions within the unit cells. The simulations follow the standard Metropolis MC algorithm.[20] Starting from a disordered configuration at high temperature (well inside the paramagnetic phase), the temperature is lowered in steps $\Delta T = 0.05$ K. At each temperature, averaging is done over 5×10^5 MC sweeps, after having discarded the first 5×10^4 MC sweeps to let the system equilibrate. We obtain the heat capacity as the derivative of the magnetic energy E, and check that it agrees with the associated energy fluctuations via the relation $C = \delta E^2/(NT^2)$, where N is the number of magnetic moments.

MC data for the heat capacity C versus T for bulk DyPO$_4$ are exhibited in the top panel of Fig. 7. As expected, the ground state obtained for the bulk sample is, indeed, the simple two-sublattice AF structure known from the literature. The thick solid red line stands for a MC simulation corresponding to an exchange field $B_{\text{ex}} = 0.550$ T ($J/k_B = -1.80$ K) for the nn exchange interaction and $B_{\text{dip}} = 0.237$ T for the dipolar field from all neighbors, giving a total interaction field of 0.787 T acting on a reference spin (the dipolar field from nn neighbors only is 0.346 T). These numbers agree quite well with published results in the literature.[5,19] The calculated heat-capacity curve is seen to coincide nicely with the experimental bulk data. It is worth mentioning that a MC simulation in which only an effective exchange interactions between nearest neighbors is assumed, that is, not including the dipolar terms, likewise reproduces the experimental results reasonably well, yielding an effective nn exchange interaction constant $J/k_B = -2.50$ K (thin solid green line in Fig. 7, top). The explanation for this result can be traced to the remarkable property of this material as cited above, that is, the near cancellation of further neighbor (exchange plus dipolar) interactions.

For the DyPO$_4$ nanoparticles, the MC simulation yields the dotted blue line plotted in the same figure if the dipolar interactions are included and the value $J/k_B = -1.80$ K found for bulk is taken for the nn exchange. Similarly, as in the experiment and as expected for a finite system, a broad anomaly is found, instead of the λ-type peak found
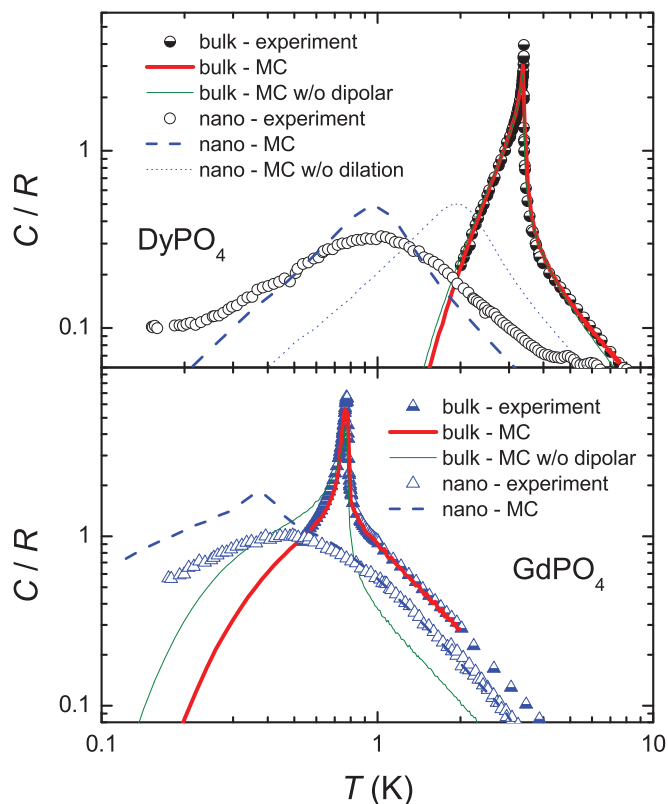
FIG. 7. (Color online) Temperature dependence of the experimental ZF magnetic heat capacities for $DyPO_4$ (top) and $GdPO_4$ (bottom) for both nanoparticles and bulk, compared to the MC simulations (lines) explained in the text.

for the bulk case. The maximum of the anomaly, however, is then centered at a temperature $T \simeq 2$ K instead of $T \simeq 1$ K as in the experiment (cf. Fig. 3). MC averages taken over particles with a size distribution of $\delta d/d = 0.2$ and mean size $d = 2.6$ nm do not change appreciably this finding. Guided by the experimental indications for a strong reduction of the magnetic interaction in the nanoparticles, as discussed above, we performed simulations on dilated samples, assuming a 12th-power decay of the nn exchange with increasing nn distance.[21–25] Much better agreement was indeed obtained for lower values of J/k_B. In particular, the thick dashed blue line in the top panel of Fig. 7 stands for results obtained for a dilation of the crystal lattice parameters by about 7%, which gives $\tilde{J}/k_B = -0.44$ K (exchange field $B_{ex} = 0.135$ T). The dipolar field due to all neighbors is now obtained as $B_{dip} = 0.116$ T, giving a total interaction field of 0.252 T instead of the 0.787 T found for bulk. This reduction by a factor of three of the total magnetic interaction in the nanosample agrees quite well with the analysis of the field-dependent heat-capacity data discussed above, from which the value 0.27 T was deduced for the total magnetic interaction field. As mentioned before, the combination of lattice expansion in the nanoparticles, lattice defects, and missing magnetic neighbors near the surface of the particles should explain the lower effective value for the magnetic interactions in the nanoparticles.

We next turn to the MC results for $GdPO_4$. As noted above, the magnetic data taken on the bulk single crystal

presented in the Appendix show a strong preference for the moments to lie in the ab (xz) plane with the b direction as the easiest axis. For this reason, an easy-plane-type uniaxial anisotropy term $-D \sum_i (S_i^y)^2$ was included in the Hamiltonian of Eq. (5.1) (with $D < 0$). We note that, although, generally speaking, crystal-field effects will be small for Gd^{3+} compounds, the Gd^{3+} ion being in an $^8S_{7/2}$ ground state, the crystal-field anisotropy can nevertheless become important in compounds with sufficiently small exchange interactions, such as the present material. We recall that for the closely related compounds $GdVO_4$ and $GdAsO_4$ a uniaxial anisotropy term with $D/k_B = 0.03$ K has been reported.[26] With $S = \frac{7}{2}$ the corresponding anisotropy energy amounts to $DS^2/k_B = 0.37$ K, quite comparable to the T_N value of $GdPO_4$.

Our MC results for the heat capacity of bulk $GdPO_4$ are in good agreement with experiments for $D/k_B = -0.081$ K and an exchange field of 0.435 T, directed along the z axis (solid black line in Fig. 7, bottom). This would correspond to a nn exchange constant $z\tilde{J}/k_B = -0.084$ K. In this configuration, the components $[B_{dip}^x, B_{dip}^y, B_{dip}^z]$ of the dipolar field (in teslas) are found to be [0.019, 0.044, 0.354]. The ground state obtained is that of a compensated antiferromagnet, since two of the four Gd^{3+} moments of a given unit cell are pointing up and the other two are pointing down (along the $z = b$ axis). Nevertheless, the magnetic ground state is rather peculiar in that, of the six nearest neighbors of a given Gd^{3+} spin that is pointing up, only four are pointing down and two are pointing up, and hence $\tilde{z} = 2$ (calculations assuming inequivalent exchange constants for different nn neighbors would become rather complicated and were not attempted). We further note that, when the anisotropy term is omitted, it is found that exchange plus dipolar interactions push the spins onto a plane perpendicular to b, with the a axis as the most preferred. Finally, simulations considering only dipolar interactions resulted in AF configurations favoring the ab plane. Thus, only the combination of the planar anisotropy term together with the exchange plus dipolar terms resulted in an AF ground state with spins pointing along the b axis, as observed experimentally. Last, results obtained by considering only nn exchange interactions, that is, leaving out the dipolar terms, yielded the thin solid red line in the same figure, with the value $z\tilde{J}/k_B = -0.098$ K. The observed strong disagreement of this calculation with the experimental data shows unambiguously the crucial importance of the inclusion of the dipolar contributions to the heat capacity, in particular as concerns the T^{-2} tail at temperatures above T_N.

Similarly, as for the $DyPO_4$ nanoparticles, we have explored in our MC calculations different values for the dilation of the crystal lattice parameters for the $GdPO_4$ nanoparticles in order to get the maximum of the broad heat-capacity anomaly at a temperature in agreement with the experimental one. Comparably good fits could be obtained for varying combinations of a small degree of dilation and the strength of the anisotropy. The MC curve shown as the dashed line in the bottom panel of Fig. 7 has been calculated adopting a dilation of about 5%, which results in $z\tilde{J}/k_B \simeq -0.047$ K, and adopting an anisotropy parameter of the same order as in the bulk sample. In this calculation, the components of the exchange field and dipolar field in the ground configuration

were found to be $[B_{\text{ex}}^x, B_{\text{ex}}^y, B_{\text{ex}}^z] = [0.044, 0.0003, 0.119]$ and $[B_{\text{dip}}^x, B_{\text{dip}}^y, B_{\text{dip}}^z] = [0.060, 0.051, 0.166]$, respectively.

VI. μSR RELAXATION STUDIES

Size effects on the spin dynamics of magnetic nanoparticles are of considerable interest from both a fundamental and application point of view, and few experimental studies have been performed to date. We, therefore, decided to study in addition to the thermodynamic behavior the spin dynamics in our samples by performing ^{31}P-NMR studies and μSR experiments. Whereas the NMR experiments were done in high magnetic fields (9.4 and 5.6 T) for reasons of sensitivity, the μSR experiments (in longitudinal geometry) have the advantage that they can be done in ZF or in a small LF (B_L), thus providing most valuable information complementary to the NMR data. We first discuss and analyze the μSR data, postponing the NMR results to the following section.

The μSR spectra were taken at variable temperatures down to 0.04 K at the ISIS facility. To correct for a possible muon response coming from the TEHP ligands, measurements were also performed on structurally and morphologically similar YPO$_4$ nanoparticles. The depolarization was then found very small and temperature-independent; see, for example, the μSR spectra collected for three representative temperatures in Fig. 8. Therefore, any contribution coming from the TEHP ligands can be safely neglected in what follows. We recall that depolarization of the muon spins in magnetic systems can result from a combination of *dephasing*, due to a distribution

FIG. 8. Zero-field μSR spectra collected at the indicated temperatures for nanoparticles of YPO$_4$.

in the static magnetic (dipolar) fields exerted at the muon sites by neighboring electronic or nuclear magnetic moments, and *relaxation* arising from dynamic fluctuations of these hyperfine fields.[27] Here the distinction between static and dynamic is determined by the time scale of the μSR experiment, which is of the order of 1 to 10 μs. In our magnetic samples, a transition from the dynamic to the static regimes is expected as the temperature is lowered. In the paramagnetic regime, the hyperfine fields from the electron spins will be rapidly fluctuating due to electron spin-lattice relaxation (ESLR) and/or electron spin-spin interactions of exchange and dipolar origin. In the long-range ordered magnetic state of the bulk sample, as well as below the freezing points of the nanoparticle moments, the fluctuations slow down to below the muon frequency window as the (quasi)static regime is reached.

Starting with the data for bulk-GdPO$_4$, ZF-μSR spectra taken at two representative temperatures above and below $T_N = 0.77$ K are shown in Fig. 9 (top panel). We find the time evolution of the depolarization (the asymmetry) for $T > T_N$ to be well described by the function

$$P_z(t) = P_z(0) G^{KT}(t, \sigma) \, e^{(-\lambda t)}. \qquad (6.1)$$

Here G^{KT} is the Kubo-Toyabe function, representing the depolarization arising from a distribution (of half width at half maximum $\Delta = \sigma/\gamma_\mu$) in the static local fields experienced by the muons, and λ is the μSR rate associated with the dynamic fluctuations of the hyperfine fields exerted by the Gd^{3+} electronic spins.[27] We recall that the Kubo-Toyabe function is defined as

$$G^{KT}(t) = \left\{ \frac{1}{3} + \frac{2}{3} [1 - (\Delta t)^\alpha] e^{\left[\frac{-(\Delta t)^\alpha}{\alpha} \right]} \right\}.$$

The concentrated limit is best described by a Gaussian distribution, for which $\alpha = 2$, whereas in the dilute limit the correct distribution function is a Lorentzian, with $\alpha = 1$. We note that values of α between 1 and 2 are often found in the literature.[28] The static contribution is, in this case, attributed to local fields arising from the nuclear moments surrounding the muon. It is found to be temperature-independent for $T > T_N$, the fit in this range yielding $\sigma_G = 0.28 (\mu s)^{-1}$ for the width of the Gaussian distribution. Keeping this value fixed leaves the relaxation rate λ as the only remaining free parameter, and the temperature dependence of this quantity resulting from the fits is given in the bottom panel of Fig. 9. It is seen that λ remains fairly constant down to $T \approx 2T_N$, then decreases rapidly to a low-valued plateau that is reached below $T \approx T_N$, suggesting the dynamical relaxation component to become decoupled due to the (static) internal fields arising from the ordering of the Gd^{3+} moments below T_N.[29] Measuring in applied LFs B_L at temperatures above 2 K reveals, indeed, that decoupling occurs for fields exceeding 5 mT, much smaller than the dipolar hyperfine fields expected in the magnetically ordered state. The temperature-independent value of about 5 MHz found for the damping rate above 2 K is in good agreement with the estimated exchange-narrowed hyperfine broadening due to electron spin-spin interactions. Similar to the longitudinal nuclear-spin-lattice relaxation rate in NMR (see Sec. VII), the μSR rate will be given by the formula[30]

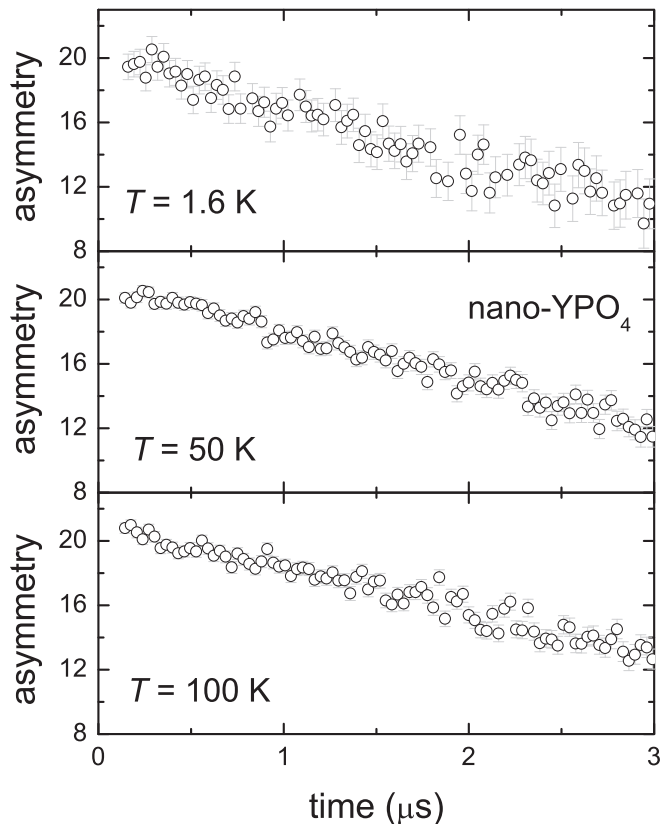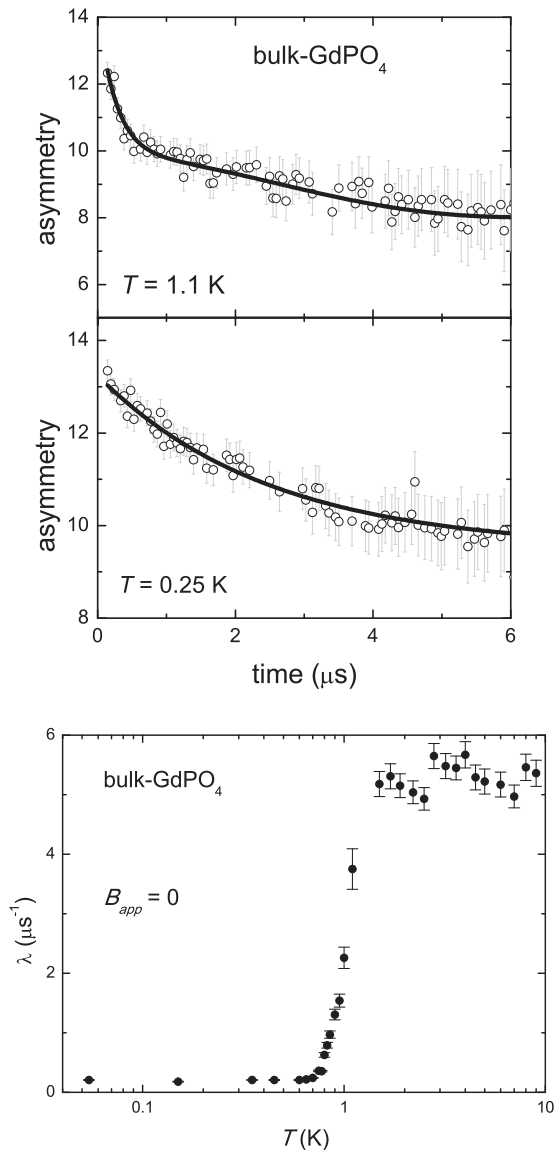$$\lambda = (2\pi)^{1/2} (\gamma_\mu B_{hf})^2 / 3\omega_{\text{ex}}. \qquad (6.2)$$

FIG. 9. (Top) Zero-field μSR spectra collected at the indicated temperatures for bulk GdPO$_4$. Solid curves are fits of the data to the Gaussian Kubo-Toyabe function, as described in the text. (Bottom) Temperature dependence of the ZF muon relaxation rate as obtained from the fits to the spectra.

Here $S = \frac{7}{2}$ is the Gd^{3+} spin, $\gamma_\mu = 8.516 \times 10^8$ Hz/T is the gyromagnetic ratio of the muon, B_{hf} is the dipolar hyperfine field at the muon site from the Gd^{3+} spins, and ω_{ex} is the exchange frequency, which is related to the Gd^{3+}-Gd^{3+} spin-spin interaction J/k_B by $\hbar\omega_{\mathrm{ex}} = |J|(2zS(S+1)/3)^{1/2}$. With $z = 6$ and $J/k_B \simeq 0.01$ K, as found above, one obtains $\omega_{\mathrm{ex}} \simeq 1.5 \times 10^{10}$ rad s^{-1}. From the experimental value $\lambda \approx 5.5$ MHz, the dipolar hyperfine field at the muon site is calculated as $B_{hf} \approx 0.36$ T, which is just equal to the dipolar field at the Gd^{3+} site in the bulk crystal calculated in the MC simulations. Unfortunately, the position of the muon is not known precisely, so the agreement may be accidental. However, in the NMR section below we shall find the same value for the dipolar hyperfine field seen by the ^{31}P nuclei in the bulk GdPO$_4$ sample.
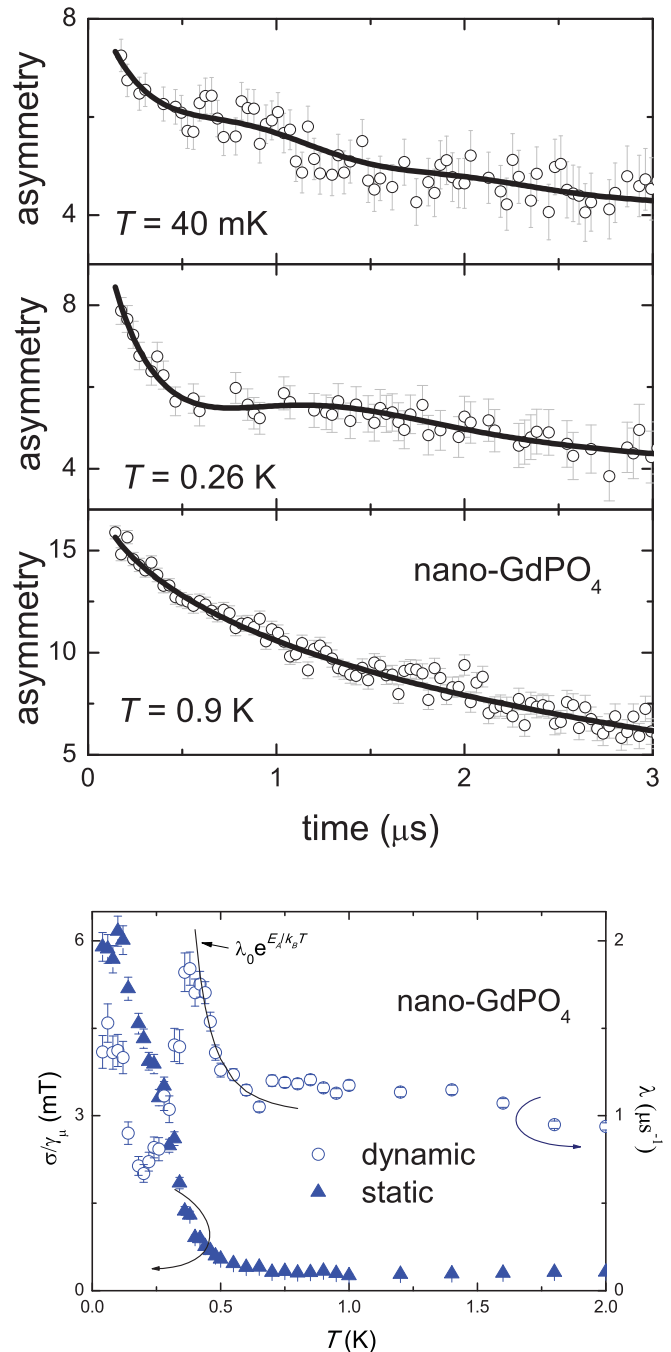

FIG. 10. (Color online) (Top) Zero-field μSR spectra collected at the indicated temperatures on GdPO$_4$ nanoparticles. Solid curves are fits to the data as described in the text. (Bottom) Temperature dependence of the static local field σ/γ_μ seen by the muons and the muon relaxation rate λ as obtained from the fits to the spectra. The solid line is the exponential increase of λ with lowering T for 0.3 K < T < 0.7 K, see text.

As clearly seen from the (representative) ZF-μSR spectra shown in Fig. 10 (top panel), the behavior found for the GdPO$_4$ nanoparticles is drastically different. The spectra for $T > 1$ K, that is, far above the freezing point of 0.2 K observed in the ac susceptibility, are predominantly exponential with a fast decay, indicating rapidly fluctuating random fields at the muon sites. The shape of the curves appears consistent with what

one would expect for a paramagnetic system, that is, when no static field is present. Below about 0.5 K, the spectra are seen to change drastically. As exemplified by the spectra taken at the low temperatures of $T = 40$ and 260 mK (top panel in Fig. 10), the depolarization does not decay monotonically. Similar as for the bulk spectra, such a nonexponential decay can be described by the Kubo-Toyabe function and indicates the gradual development of a static internal field experienced by the muons, leaving only one degree of freedom along the longitudinal direction. We note, however, that the gradual decay of the $\frac{1}{3}$ tail observed at longer times indicates that not all the particle moments are blocked within the time window of the muon probe, even at 40 mK. The overall temperature dependence exhibits the same characteristic behavior as observed for a spin-glass system.[27] The spectra could be well fitted to Eq. (6.1) assuming a Lorentzian distribution of the static internal fields, as expected for a diluted magnetic system. The resulting temperature dependencies of the half width at half maximum of the Lorentzian field distribution experienced by the muons (σ/γ_μ) and the μSR rate λ are shown in the bottom panel of Fig. 10. One observes a gradual transition to the frozen spin state, similar to that found in the ac susceptibility at the (frequency-dependent) freezing temperature $T_f \simeq 0.2$ K. Upon cooling below about 0.7 K, the μSR rate starts to increase. At about 0.4 K–0.5 K, a static local field develops, and its value extrapolates to about 6 mT for $T \to 0$, while concomitantly λ drops sharply (Fig. 10). Above 0.7 K, the rate remains nearly temperature independent, similar to the effect found for the bulk sample but now at a value of 1 MHz, that is, about five times lower. We attribute the μSR above 0.7 K to the same mechanism as in the bulk, namely, the fluctuations of the Gd^{3+} spins inside the particles due to the Gd^{3+}-Gd^{3+} spin-spin interactions. Using Eq. (6.2) and noting that the J value found in the MC calculations for the nanoparticles is about a factor of two lower than in the bulk, one would expect the average dipolar hyperfine field B_{hf} in the particles to be a factor of $\sqrt{5.5 \times 2} \simeq 3.3$ smaller than in the bulk, which very nicely agrees with the values of $B_{\text{dip}} \simeq 0.1$ T and 0.36 T for nanoparticles and bulk $GdPO_4$, respectively, reported above in the MC calculations and heat capacity analyses. In the NMR section below, we shall encounter a similar reduction of the dipolar hyperfine field at the ^{31}P nuclei when going from the bulk $GdPO_4$ to the nanoparticles.

Guided by the results from the susceptibility and heat capacity, the μSR data found below 0.7 K can thus be explained as follows.[31,32] When the bulk magnetic ordering temperature is approached below 1 K, the Gd^{3+} electronic spins inside each particle become (at least to large extent) ordered antiferromagnetically, implying that the high-temperature relaxation channel for the μSR arising from the intraparticle spin-spin interactions gradually disappears. Instead, a new relaxation channel appears in the form of spin-lattice relaxation associated with the flipping of the net superparamagnetic moments developed at the nanoparticles. In the ac-susceptibility study, this superparamagnetic relaxation was found to be described by the Arrhenius law, with a relaxation time $\tau = \tau_0 \exp(E_A/k_B T)$, with an activation energy $E_A/k_B = 2.3$ K and $\tau_0 \approx 5.6 \times 10^{-10}$ s. In the fast fluctuating

limit, that is, when $1/\tau$ is much faster than the typical muon precession frequency, the μSR rate is just proportional to τ, namely, $\lambda = 4\sigma_L^2 \tau$.[31] The sharp increase in λ observed in between 0.7 K and 0.3 K can, therefore, be directly related to the exponential increase of τ with decreasing temperature, that is, $\lambda = \lambda_0 \exp(E_A/k_B T)$, depicted as the solid line in the bottom panel of Fig. 10, corresponding to $E_A/k_B = 2.3$ K and $\lambda_0 \approx 300$ s^{-1}. As the freezing temperature is approached, however, these fluctuations become slow compared to the μSR time scale and the (quasi-)static regime is entered (below about 0.3 K). In the static limit, the damping rate is simply given by σ_L, and from the $T \to 0$ extrapolated value of 6 mT for σ_L/γ_μ in Fig. 10, bottom panel, one calculates $\lambda(T = 0) \approx 0.8$ MHz, in good agreement with the lowest observed experimental λ value. The temperature range at which the transition from the dynamic to the static regime should occur can be roughly estimated by equating the just mentioned dynamic and static expressions for λ, predicting this to happen when $\lambda \approx 1/4\tau$. From the value of 2 MHz reached by λ at the maximum, this should correspond to the temperature at which $\tau \approx 0.125 \times 10^{-6}$ s. From the Arrhenius law, one then calculates a temperature of 0.43 K for the transition, in reasonable agreement with the position of the maximum in λ found experimentally ($\approx$0.37 K). The higher value of the freezing temperature observed here in the μSR data as compared to 0.2 K in the frequency-dependent ac-susceptibility, is thus simply due to the much shorter μSR time scale as compared to the frequencies in the χ_{ac} experiment, and we can fit the freezing temperatures derived from the susceptibility as well as from the μSR data in a single Arrhenius plot, as shown in Fig. 2, with the mentioned activation energy of $E_A = 2.3$ K and $\tau_0 = 5.6 \times 10^{-10}$ s. Finally, the upturn observed at the lowest temperatures in λ in Fig. 10, that is, below 0.2 K, is attributed to the previously mentioned fluctuations that remain even at 40 mK, arising most probably from loose spins at the surface layers of the magnetic cores.

For the case of $DyPO_4$, experiments were only performed in LFs on the nanoparticle sample. We note, however, that ZF-μSR data have been published on bulk $DyVO_4$, a material which, in several respects, resembles the $DyPO_4$ compound.[33] We did not observe any precession signal as usually associated with the presence of a static internal field, even for temperatures $T \ll T_B \simeq 1$ K. Instead, the data indicate that the muon polarization relaxes due to dynamical field fluctuations down to our lowest temperature reached, $T \simeq 40$ mK. We conclude this from the fact that (i) the depolarization shows monotonic decay without recovery to $\frac{1}{3}$ and (ii) the dependence of the depolarization on B_L is very weak, since even the highest field $B_L = 2.5$ kOe achievable in the experiment was not strong enough to decouple the signal.[29] We thus analyzed the μSR data in terms of ESLR. Within this context, the previously noted square root-exponential decay $\propto \exp[-(\lambda t)^{0.5}]$ is expected in the fast fluctuation limit.[34] The fit to this function was found satisfactory at all temperatures, as illustrated in the top panel of Fig. 11 for some representative temperatures. In the bottom panel of the same figure, the temperature dependence of the thus-obtained ZF muon longitudinal relaxation rate λ is plotted.

As can be seen in Fig. 11 (bottom), we have to account for two maxima in $\lambda(T)$, a pronounced one at about ~35 K
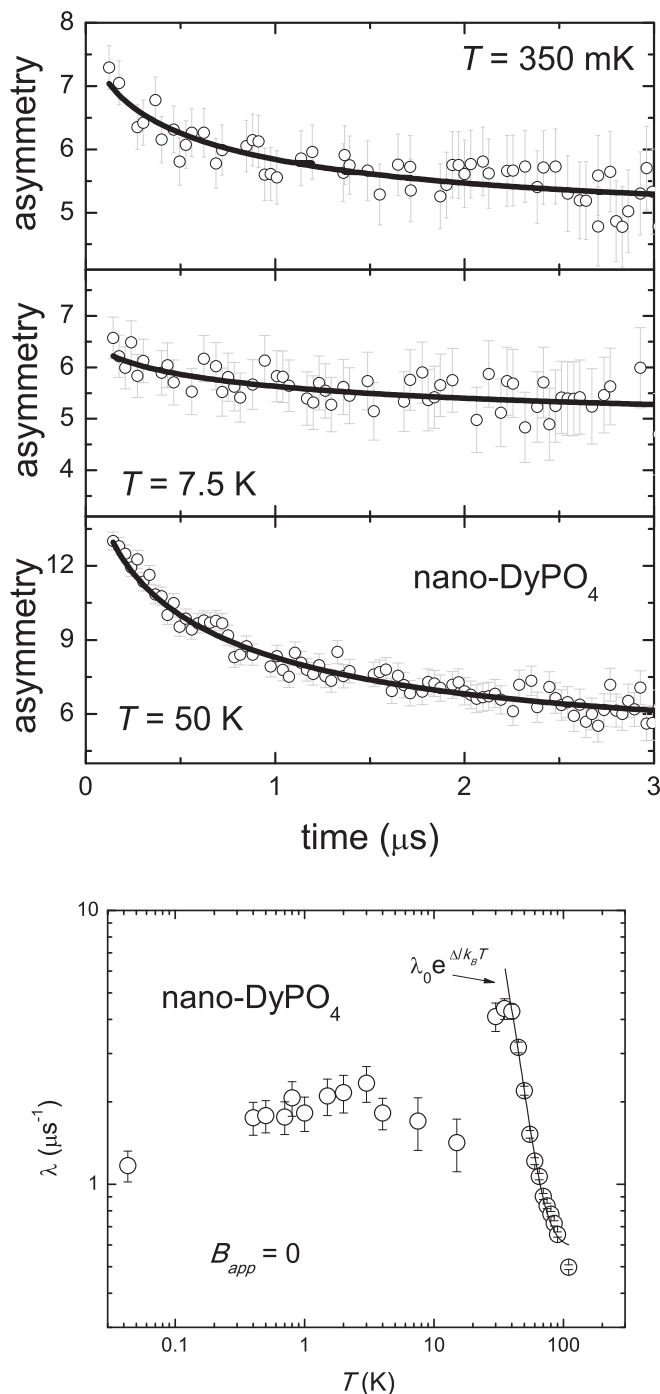
FIG. 11. (Top) Zero-field μSR spectra collected at the indicated temperatures on DyPO$_4$ nanoparticles. The solid curves are fits of the data as described in the text. (Bottom) Temperature dependence of the muon relaxation rate as obtained from the fits to the spectra. The solid line is the exponential fit to the higher-temperature data (see text).

and a weaker and broader one in the 1 K–4 K temperature range. We will explain the high-T peak in terms of spin-lattice relaxation of the individual Dy^{3+} spins, whereas the low-T feature is attributed to the superparamagnetic blocking process of the particles that is also observed for lower frequencies in the ac susceptibility. Indeed, the low-temperature part of the

μSR rate is seen to be similar to that found for the GdPO$_4$ nanoparticles, although the maximum is, in this case, much less pronounced. Recalling that for the DyPO$_4$ nanoparticles the superparamagnetic blocking in the susceptibility is described by the Arrhenius law $\tau = \tau_0 \exp(E_A/k_B T)$, with activation energy $E_A = 10$ K and $\tau_0 \approx 4 \times 10^{-10}$ s, we estimate the expected temperature of the maximum in λ with the same criterion as used above, that is, when $\lambda \approx 1/4\tau$. Noting that the maximum value reached here by λ is again about 2 MHz, we then find this relation to be satisfied for $T \approx 2$ K, in accord with the temperature range where the transition takes place in Fig. 11. We can, thus, fit the freezing temperatures derived from the susceptibility as well as from the μSR data in a single Arrhenius plot, as shown in Fig. 2. The fact that the transition anomaly is much less pronounced as compared to the GdPO$_4$ case can be attributed to the higher degree of magnetic disorder inside the DyPO$_4$ nanoparticles as found in the above. The much larger amount of missing magnetic neighbors implies a broader distribution in the E_A values for the DyPO$_4$ nanoparticles and, thus, in the associated freezing temperatures. Moreover, the amount of spin fluctuations remaining present even far below the blocking temperature will also be much larger, explaining the high value for λ found at our lowest temperature ($\sim$1.8 MHz instead of $\sim$0.6 MHz for the GdPO$_4$ case). The higher value for the blocking temperature in the μSR, about 2 K–3 K compared to 1 K in the ac susceptibility, can again be simply attributed to the much shorter μSR time scale as compared to that of the χ_{ac} data.[32]

As mentioned, we interpret the high-temperature dependence of λ seen in Fig. 11 in terms of the fluctuations of the individual Dy^{3+} spins originating from electronic spin-lattice relaxation (ESLR).[35] Assuming Lorentzian (single exponential) relaxation for the electron spins, the relation between λ and the electronic relaxation time τ_e is given more generally by

$$\lambda = 2(\gamma_\mu B_\perp)^2 \frac{\tau_e}{1 + \omega_L^2 \tau_e^2}, \qquad (6.3)$$

with $\omega_L = \gamma_\mu B_L$ the angular muon frequency corresponding to B_L, and $B_\perp$ is the magnitude of the perpendicular component of the fluctuating dipolar hyperfine field. Since we are in the fast-fluctuating limit and measure in ZF, that is, $\omega_L = 0$, this equation reduces to $\lambda = 2(\gamma_\mu B_{hf})^2 \tau_e$ for the present case. We show in Fig. 11 as the solid curve, the calculated contribution to $\lambda(T)$ from ESLR, taking for $\tau_e(T)$ the data obtained by Forester and Fernando from Mössbauer spectra (in ZF) in the range 10 K–100 K.[36] They attributed the observed relaxation to an Orbach process involving the excited level at ≈ 110 K, resulting in an exponential decrease of τ_e with temperature given by $\tau_e = \tau_0 e^{\Delta/k_B T}$, with $\tau_0 = 5 \times 10^{-11}$ s and $\Delta = 110$ K. Here Δ is the energy separation between the ground doublet and the first excited doublet of the Dy^{3+} electron spin. With an average hyperfine field of $B_\perp = 50$ mT, this predicts an exponential dependence of λ given by $\lambda(T) = \lambda_0 e^{\Delta/k_B T}$, with $\lambda_0 = 2 \times 10^5 s^{-1}$ and the above value for Δ. As seen in Fig. 11, this prediction fits the experimental data remarkably well in the whole range above the maximum. This strongly indicates that the energy distance between the two lowest doublets is indeed comparable to what is known for the bulk. We note that the value obtained here for $B_\perp$ is comparable to the dipolar field of

about 120 mT at the Gd^{3+} site obtained in the MC calculations. Below about 30 K, the τ_e becomes of the order of the muon frequency, explaining why λ goes through a maximum. Below about 10 K, the fluctuations of the individual Dy^{3+} spins due to ESLR have become much too slow; their contribution to λ decreases and the relaxation by the collective fluctuations of the Dy^{3+} spins in each particle due to superparamagnetic relaxation becomes the most important process.

VII. ^{31}P NMR STUDIES

As mentioned above, we have further studied the Gd^{3+} and Dy^{3+} spin dynamics by performing ^{31}P-NMR studies on powdered samples of both nanoparticles and bulk in fields of 9.4 and 5.6 T. In the NMR data at 9.4 T the ^{31}P-NMR signal is found to be centered around 162 MHz, with linewidths of a few MHz at room temperature. For the nanoparticles the linewidth starts to increase linearly with inverse temperature below $\lesssim$200 K. The broadening arises most likely from inequivalent rare-earth sites in the nanocluster cores, the corresponding envelope signals being exchange-narrowed at high temperatures. For all four samples, the temperature dependencies of the ^{31}P-nuclear spin-lattice relaxation (NSLR) time T_1 were measured at the center of the line.

Data obtained on the $GdPO_4$ samples are shown in Fig. 12. Over a large temperature range, the curves for both nanoparticles and the bulk material are flat, indicating an analysis in terms of exchange narrowing to be appropriate, similar to that applied to the μSR data. The difference is that, in this case, we have to take into account the presence of the large (9.4 T) NMR field, that is, much larger than the exchange field (0.4 T) associated with the Gd^{3+}-Gd^{3+} spin-spin interaction. Accordingly, the data are interpreted by means of the formula

$$1/T_1 = (2\pi)^{1/2} \left(\gamma_n^2 B_{hf}^2 / 3\omega_{ex} \right)(1 - \tanh^2 X),$$

where $X = g\mu_B S B_{app}/k_B T$ and B_{app} is the applied field. The main difference between the formula for the ZF case [Eq. (6.2)] is thus the factor $(1 - \tanh^2 X)$ that takes into account the effect
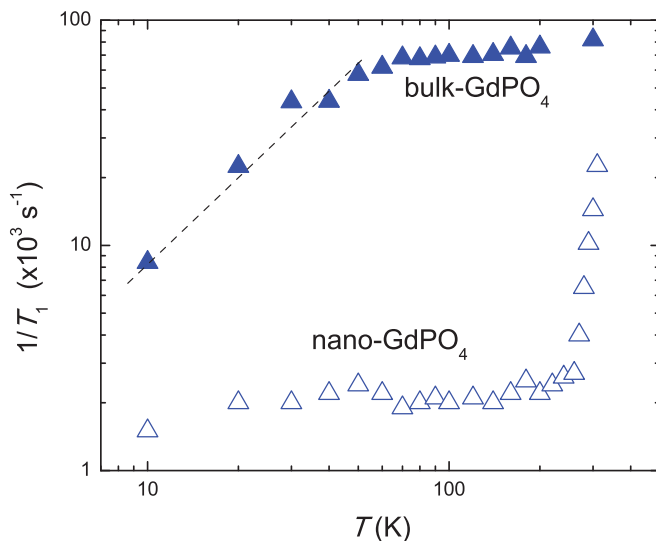
of the polarization of the electron spins at low temperatures by B_{app}. When the electron spins become polarized, they can no longer take up energy from the nuclear spins, leading to an exponential decrease of the nuclear $1/T_1$ of the form $\exp(-X)$. In the present case, the applied field of 9.4 T will split the Gd^{3+} $S = \frac{7}{2}$ multiplet over an energy span of 44 K. Thus, one may, indeed, expect a decrease in $1/T_1$ to start below about 50 K, that is, when the depopulation of the upper spin levels starts. The exponential decrease is clearly visible in the bulk data (see the dashed curve in Fig. 12). In the nanoparticle sample, the decrease is much less pronounced, which points to an additional source of fluctuations remaining active even at low temperature. We recall that the μSR study also revealed the presence of appreciable fluctuations even at about 40 mK. This suggests the magnetic disorder in the nanoparticles due to missing neighbors at the surface as a possible explanation. The strong increase observed for the nanosample $1/T_1$ above about 250 K is probably also a surface effect; we attribute it tentatively to additional fluctuations induced by thermal motions of the outer atoms in the particles.

Apart from the field term, the only difference in the formulas for λ and $1/T_1$ is the different gyromagnetic ratio for the muon and for the ^{31}P nucleus, for which $\gamma_n = 2\pi \times 1.723 \times 10^7$ Hz/T, giving a ratio $(\gamma_\mu/\gamma_n)^2 = 62.2$. This predicts the (temperature independent) values obtained for λ and $1/T_1$ to be in this same ratio, which is indeed observed in the case of the bulk sample, for which we find $\lambda \approx 5.5$ MHz and $1/T_1 \approx 0.08$ MHz (see Fig. 12). We conclude that, as regards the bulk sample, the experiment shows the dipolar hyperfine fields at the muon site and at the ^{31}P nucleus to be equal within the errors involved (about 0.36 T, as in the MC calculations). For the nanosample, the temperature-independent value of $1/T_1$ is $\approx$35 times smaller than in bulk (Fig. 12). Noting as before that ω_{ex} is directly proportional to $|J|$ and hence is about half that in bulk, we would expect a $\sqrt{35 \times 2} \simeq 8.3$-times smaller dipolar hyperfine field in the nanosample. Thus, the reduction of the dipolar field at the ^{31}P nucleus in the nanoparticles as compared to bulk appears to be a bit larger than the corresponding reduction at the muon site.

As in the case of the μSR data, in case of $DyPO_4$ the analysis of the NMR data should be done in terms of ESLR. Unambiguous conclusions are, however, hardly possible because of the complications inherent in a field-dependent study on a powder sample of such an anisotropic magnetic system. From the inelastic neutron-scattering data on bulk $DyPO_4$,[7] it was concluded that the distances in energy (in ZF) of the first five excited doublets above the ground-doublet are given by 99 K, 110 K, 186 K, 211 K, and 259 K, the remaining two doublets lying at about 440 K. The doublets will be split considerably by the large B_{app}, in particular along the directions of large g values, and as a consequence of the (strongly) anisotropic properties, the amount of splitting will depend heavily on the orientations of the crystallites in the powder. Consequently, the mutual distances of the levels will vary. Even when restricting the analysis to the temperature range below 100 K, where only the first two excited doublets will be appreciably populated, one encounters the difficulty that the admixtures of the excited states in the ground doublet will depend on the orientation, since the amount of mixing depends on the square of the interlevel distances. Taking as our example the direct process

FIG. 12. (Color online) Temperature dependence of ^{31}P-NSLR rates for $GdPO_4$ nanoparticles and bulk, as labeled.

for the ESLR of a ground-state Kramers doublet in the presence of a nearby excited state, the full expression for the ESLR rate $1/\tau_e$ is given by[15]

$$\tau_e^{-1} = R_{\mathrm{dir}}\hbar\omega^5 \coth\left(\frac{\hbar\omega}{2k_B T}\right), \qquad (7.1)$$

where $R_{\mathrm{dir}} = 3V^2/2\pi\rho v^5\hbar^4\Delta^2$, $\hbar\omega = g\mu_B B_{\mathrm{app}}$, and $\Delta \approx 100$ K is the energy separation to the nearest excited level. V is the matrix element between the two levels of the ground Kramers doublet.[15] Of particular importance here is that for a Kramers ground doublet $V \neq 0$ only through the admixture of excited levels by B_{app}, implying that the ESLR rate will vary strongly with orientation. The same is true for the above-mentioned Orbach process, which does not depend directly on the field but only indirectly, since it depends exponentially on the interlevel separation, which will vary with orientation. All of this implies that only a few qualitative conclusions can be drawn from the data obtained here.

As shown in Fig. 13, between 140 K and 200 K, the temperature dependence of the ^{31}P-NSLR rate is (much) stronger in the bulk than in the nanoparticles. Interestingly, both nanoparticle and bulk samples show a broad maximum at about the same $T_{\max} \approx 40$ K. As noted above, we assume the nuclear relaxation to arise from fluctuations of the individual Dy^{3+} spins induced by ESLR, which produce fluctuating hyperfine fields on the nearby ^{31}P nuclei. Assuming single exponential relaxation for the ESLR, the nuclear T_1 can be related to the ESLR time τ_e by the well-known expression

$$T_1^{-1} = A^2 \frac{\tau_e}{1 + \omega_L^2 \tau_e^2}. \qquad (7.2)$$

Here $A = \gamma_n B_\perp$ gives the amplitude of the (transverse component of) the fluctuating hyperfine field and $\omega_L \approx 1 \times 10^9$ Hz is the ^{31}P-NMR Larmor frequency corresponding to the applied field of 9.4 T. In the high-T/fast-fluctuation limit ($\omega_L\tau_e \ll 1$), one has $T_1^{-1} \approx A^2\tau_e$, whereas in the opposite limit $T_1^{-1} \approx A^2/\omega_L^2\tau_e$. Above the maximum, occurring for
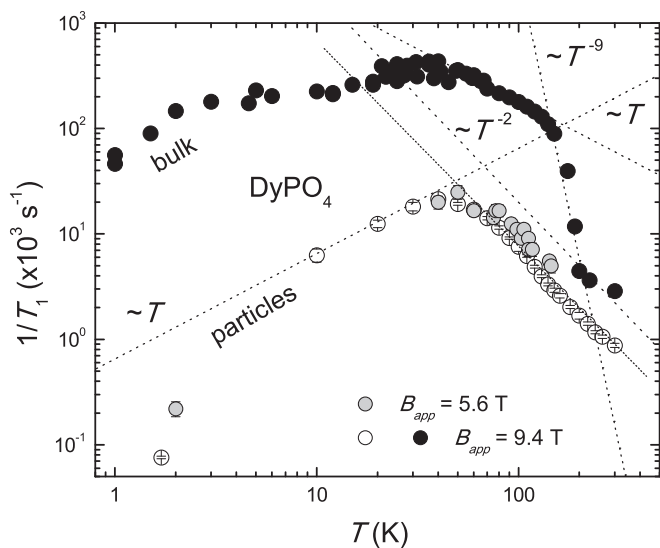

FIG. 13. Temperature dependence of ^{31}P-NSLR rates for DyPO$_4$ nanoparticles and bulk, as labeled. The dotted curves show the different temperature dependencies of the rates discussed in the text.

$\omega_L \approx \tau_e$, the temperature dependence of the nuclear T_1^{-1} for the nanoparticles can be well reproduced by taking for the ESLR rate a quadratic dependence on temperature, that is, $\tau_e^{-1}(T) \propto aT^2$, which would correspond to the high-T limit of the two-phonon Raman process (for $T > \Theta_D$).[15] This then leads to $T_1^{-1}(T) \propto T^{-2}$ in this range. Quantitatively, the fit shown in Fig. 13 involves for the prefactor a the value $a = 6.27(19) \times 10^5$ K^{-2} s^{-1} down to $\approx$60 K, which would imply the Debye temperature of the nanoparticles to be of order 50 K, that is, a factor of three lower than in the bulk. Below the maximum in the $T_1^{-1}(T)$, the high-T limit of the direct process, that is, $\tau_e^{-1} \propto T$, appears to become the dominating contribution since, in the range 10 K–40 K, one observes that $T_1^{-1}(T) \propto T$.

For bulk DyPO$_4$, the T_1^{-1} data at highest temperatures ($>$200 K) in Fig. 13 also show the T^{-2} dependence attributed to the high-temperature Raman process, although with a factor of four faster rate. Below 200 K, the temperature dependence changes drastically to $\propto T^{-9}$, which is, in fact, the dependence expected on basis of the ESLR two-phonon Raman process for temperatures $T < \Theta_D$.[15] The crossover temperature of about 200 K is, indeed, not too far from the $\Theta_D = 150$ K found above from the bulk heat capacity. At $\approx$140 K, a second crossover is seen to occur where the rate appears to become governed by the high-temperature limit of the direct process for ESLR; that is, $\tau_e^{-1} \propto T$ and thus (above the maximum) $T_1^{-1} \propto T^{-1}$. The fact that the T^{-9} term is not observed for the nanoparticles in the same temperature range as in the bulk would, therefore, be in agreement with the much lower Θ_D value of about 50 K. We thus ascribe the broad maximum (at which $\omega_L \approx \tau_e$) found at about the same temperature of 40 K for both nanoparticles and the bulk to the direct process for the ESLR of the Dy^{3+} Kramers doublets. We finally note that the decrease of the nuclear T_1^{-1} below the linear term observed for both nanoparticles and bulk at lowest temperatures (below 3 K) is probably due to the above-discussed effect of the polarization of the electronic spins, occurring when $k_B T \ll g\mu_B B_{\mathrm{app}}$ (the term $[1 - \tanh^2(\hbar\omega/2k_B T)]$) and predicting an exponential decrease of T_1^{-1} at lowest temperatures. The decrease is particularly pronounced for the nanoparticles for which it is seen that, in agreement with this prediction, the relative decrease of T_1^{-1} is strongest in the highest (9.4 T) applied field (see data points above 2 K), whereas the data at high temperature $T \geqslant 30$ K show no appreciable field dependence.

VIII. CONCLUDING REMARKS

We have presented an extensive study of size effects in the magnetic properties of AF insulating materials, occurring when the sample sizes are reduced in volume to about 10 nm^3, in our case, corresponding to about 150 magnetic atoms per particle. The theoretically predicted suppression of the transition to magnetic long-range order familiar for the bulk samples has been evidenced most clearly by measurements of the magnetic heat capacity and susceptibility for both bulk and nanoparticle samples. Missing magnetic neighbors and surface disorder in the nanoparticles lead to net moments per particle, which in our densely packed powder samples interact via dipolar interactions and, thus, become frozen into glassy

spin states at low temperatures. By contrasting nano- and bulk samples of the well-known highly anisotropic Ising compound DyPO$_4$ with its more isotropic analog GdPO$_4$, specific effects related to the anisotropy could be distinguished.

These physical measurements were backed up by MC simulations, which proved to be very valuable by not only confirming qualitatively the trends observed, but, in addition, providing quantitative estimates of the magnetic exchange and dipolar interaction parameters, thereby supporting the experimental analysis. The simulations strongly suggest substantial reductions of these parameters in the nanoparticles, not surprising in view of the expected expansion of the lattice parameters in particles of nanometer size.

In addition to the static thermodynamic behavior, studies of the spin dynamics were performed, on one hand at low frequencies (10^2–10^4 Hz) by ac-susceptibility measurements, and on the other, at high frequencies (MHz) by (ZF) μSR experiments and (high-field) NMR relaxation experiments. The low-frequency experiments on the nanoparticles provided clear evidence for the freezing transitions occurring at low temperature and the characteristic difference in behavior between the Dy and Gd nanoparticles related to the strong Ising anisotropy of DyPO$_4$. In the high-temperature range, that is, high compared to the bulk magnetic ordering temperatures, these high-frequency dynamics probe the fluctuations due to either spin-lattice relaxation or spin-spin exchange interactions inside the particles. At low temperatures the magnetic long-range ordering in bulk and the freezing phenomena in the nanoparticles could be clearly distinguished in the μSR experiments. In quantitative respect the magnetic interaction parameters and dipolar fields obtained from the analysis of the dynamic measurements were found to be fully consistent with those derived from the MC simulations and the thermodynamic data.

ACKNOWLEDGMENTS

APPENDIX: MAGNETIC PROPERTIES OF BULK GdPO$_4$

As mentioned in the Introduction, a brief characterization of the magnetic behavior of the bulk compound GdPO$_4$ has been made by measuring the differential (ac) susceptibility along three mutually perpendicular directions of a single-crystal sample in the magnetic ordering region as a function of temperature and field (0.1 K $< T <$ 4 K; 0 $< B_{app} <$ 1 T). The results are displayed in Figs. 14(a)–14(d). Antiferromagnetic order was expected (and found) in view of the known properties of the related compounds GdVO$_4$ and GdAsO$_4$, which order

TABLE I. Compilation of exchange and anisotropy parameters for GdVO$_4$, GdAsO$_4$, and GdPO$_4$. The Néel ordering temperature, exchange field, anisotropy field, and exchange constant are denoted by T_N, B_{ex}, B_{an}, and $|J|/k_B$, respectively.

	T_N (K)	B_{ex} (T)	B_{an} (T)	$|J|/k_B$ (K)
GdVO$_4$	2.50	1.43	0.37	0.068
GdAsO$_4$	1.26	0.82	0.37	0.039(3)
GdPO$_4$	0.77	0.4	0.37	0.02

antiferromagnetically below $T_N = 2.5$ K and $T_N = 1.3$ K, respectively.[26,37–41] In Table I, a compilation has been made of the transition temperatures and the exchange and anisotropy parameters for the three compounds.

The crystal structure of GdPO$_4$ is monoclinic, space group $P2_1/n$, with lattice parameters $a = 6.643$ Å, $b = 6.841$ Å, $c = 6.328$ Å, and $\beta = 104.01°$ ($\alpha = \gamma = 90°$).[6] There are four inequivalent Gd^{3+} ions per unit cell. A given Gd^{3+} reference ion is surrounded by six nearest magnetic neighboring ions at distances varying between 4.0 and 4.2 Å. As indicated in Fig. 14(a), measurements were taken along three mutually perpendicular directions, namely, the crystallographic a and b axes and the c' direction, which is perpendicular to the ab plane and will thus make an angle of about 14° with the crystallographic c axis. As seen in Fig. 14(a), the ZF ac susceptibility is independent of direction down to 1.5 K, that is, about twice the $T_N = 0.77$ K. Above 1 K, the susceptibility is well described by the Curie-Weiss law for an antiferromagnet, $\chi = C/(T + \theta)$, with $\theta \approx 0.9$ K and $C = 7.9$ K emu/mole, as expected for $g = 2$ and $S = \frac{7}{2}$. Although the susceptibility curves in Fig. 14(a) indicate compensated antiferromagnetism (no evidence for a weak ferromagnetic moment), in none of the three directions does the susceptibility appear to vanish completely for $T \to 0$, as would be appropriate for the parallel susceptibility (parallel to the easy axis) of a simple compensated two-sublattice antiferromagnet. Thus, either the b axis is not the true parallel direction but somewhere intermediate or the AF structure is more complex, as suggested by the MC simulations. A more complex magnetic structure is, moreover, not unexpected in view of the four inequivalent Gd^{3+} sites per unit cell, leading to variations in the distances with the six nearest neighbors and, accordingly, in the magnetic interactions. No attempt was made for further refinement of the magnetic structure, however, since only a quick survey was intended in this work.

Using mean-field theory for the simple two-sublattice antiferromagnet, the exchange constant J/k_B can be estimated from the susceptibility data in two ways, that is, from the formula for the Curie-Weiss temperature $\theta = -2z|J|S(S + 1)/3k_B$ and from the value of the susceptibility reached at the Néel temperature $\chi = Ng^2\mu_B^2/4z|J|$. From $\theta \approx 0.9$ K one obtains $z|J|/k_B \approx 0.08$ K and from $\chi(T = T_N) \approx 6.8$ emu/mole one finds $z|J|/k_B \approx 0.052$ K. These values compare favorably with the ones deduced from the magnetic heat capacity (Sec. IV) and from the field-dependent susceptibility isotherms discussed below.

What can be further inferred from the data in Fig. 14(a) is that the a and b axes apparently define an easy plane, with small in-plane anisotropy and the b axis being (closest to)
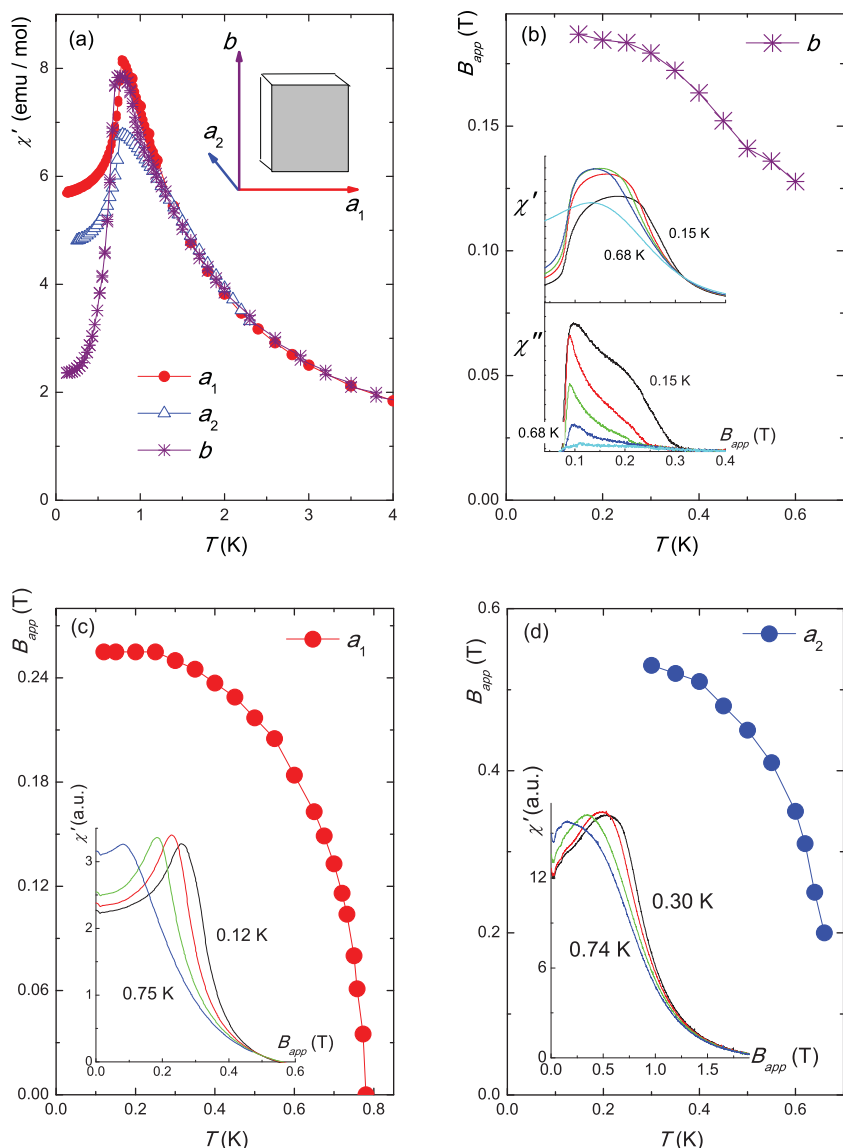
FIG. 14. (Color online) Experimental susceptibility performed on a single-crystal of GdPO$_4$. In (a) comparison between ZF ac susceptibility as a function of the direction. In (b)–(d) are shown the B_c vs T magnetic phase diagrams for fields oriented along the three directions indicated in the inset of (a), namely in (b) along the b axis (crystal symmetry axis); (c) along the a axis (perpendicular to b); (d) along the c' axis perpendicular to the ab plane. The B_c values were obtained from the χ vs B_{app} data shown in the insets.

the most preferred direction. The out-of-plane anisotropy is much larger, the c' axis being apparently the hardest direction. Further proof for this interpretation was obtained from field sweeps below T_N, in which the differential susceptibility was recorded while the dc field was swept at a slow rate of 0.05 T/min at constant temperatures. Some representative curves of susceptibility versus field are shown in the Figs. 14(b)–14(d). The real component, χ' has been plotted; only for the field parallel to the b axis the imaginary component χ'' was found to be appreciable and is also shown. The maxima in these plots (better decribed as the points where the susceptibility starts to drop steeply) should indicate the transitions from the AF phase to the paramagnetic phase. Above these field values (B_c), the associated Zeeman energies become larger than the combination of AF exchange and anisotropy energies. Plotting these B_c values as a function of temperature yields an AF phase diagram that is similar to what is expected for a two-sublattice antiferromagnet with biaxial anisotropy of the easy plane type. Indeed, the values obtained by extrapolating to $T = 0$ the critical fields B_c are almost the same when the

field is along the b axis or the a axis, namely, $B_c^{(b)} \simeq 0.24$ T and $B_c^{(a)} \simeq 0.26$ T, respectively, the latter being slightly higher, reflecting a weak in-plane anisotropy in the plane formed by these two axes. The c' axis clearly is the hardest direction, with $B_c^{(c')} \simeq 0.60$ T, reflecting the much larger out-of-plane anisotropy.

Due to the lack of more detailed experimental information, we analyze the critical fields thus determined by simple mean-field theory for the two-sublattice antiferromagnet with orthorhombic (biaxial) the anisotropy of the easy plane (XY) type. Defining the AF exchange field as $B_{ex} = 2z|J|S/g\mu_B$ and the in-plane and out-of-plane anisotropy fields as B_{an}^{in} and B_{an}^{out}, the expressions for the critical fields become $B_c^{(b)} = B_{ex} - B_{an}^{in}$, $B_c^{(a)} = B_{ex} + B_{an}^{in}$, and $B_c^{(c')} = B_{ex} + B_{an}^{out}$. Using the above experimental values for the extrapolated critical fields then yields $B_{ex} = 0.25$ T, $B_{an}^{out} = 0.40$ T, and $B_{an}^{in} = 0.03$ T. The value calculated for the exchange constant from B_{ex} is thus $z|J|/k_B = 0.05$ K, in reasonable agreement with the other determinations found above. The out-of-plane anisotropy field is of the same order as reported for the

two related Gd compounds (see Table I), but the present compound distinguishes itself in that the anisotropy is of the easy-plane instead of the easy-axis type and that the exchange field has become so small as to be of the same order as the anisotropy field. As discussed in the literature, the anisotropy in these materials arises from the combination of higher-order crystal-field effects on the Gd^{3+} ion and the

anisotropy associated with the dipolar interactions developed in the ordered phase. Last, we note that the features observed around 0.1 T in the field sweeps with the field parallel to the b axis are probably a reorientation phenomenon within the easy plane, associated with the weak in-plane anisotropy. This lower field-induced transition is most clearly observed in the imaginary component of the susceptibility.

---

*http://molchip.unizar.es/

†jongh@physics.leidenuniv.nl

[1] See, e.g., B. Barbara and E. M. Chudnovsky, Phys. Lett. A **145**, 205 (1990).

[2] See, e.g., A. E. Ferdinand and M. E. Fisher, Phys. Rev. **185**, 832 (1969); D. P. Landau, Phys. Rev. B **13**, 2997 (1976).

[3] S. Mørup, D. E. Madsen, C. Frandsen, C. R. H. Bahl, and M. F. Hansen, J. Phys. Condens. Matter **19**, 213202 (2007).

[4] A. Urtizberea, F. Luis, A. Millán, E. Natividad, F. Palacio, E. Kampert, and U. Zeitler, Phys. Rev. B **83**, 214426 (2011).

[5] J. C. Wright, H. W. Moos, J. H. Colwell, B. W. Mangum, and D. D. Thornton, Phys. Rev. B **3**, 843 (1971).

[6] C. Thiriet, R. J. M. Konings, P. Javorsky, N. Magnani, and F. Wastin, J. Chem. Thermodyn. **37**, 131 (2005).

[7] C. K. Loong, L. Soderholm, J. Simon Xue, M. M. Abraham, and L. A. Boatner, J. Alloys Compd. **207/208**, 165 (1994).

[8] W. Scharenberg and G. Will, Int. J. Magn. **1**, 277 (1971).

[9] It is, in fact, a slightly distorted diamond lattice in which each Dy^{3+} ion has four (equivalent) nearest magnetic neighbors at 3.78 Å distance.

[10] O. Lehmann, H. Meyssamy, K. Kömpe, H. Schnablegger, and M. Haase, J. Phys. Chem. B **107**, 7449 (2003).

[11] E. Suljoti, M. Nagasono, A. Pietzsch, K. Hickmann, D. M. Trots, M. Haase, W. Wurth, and A. Föhlisch, J. Chem. Phys. **128**, 134706 (2008).

[12] T. G. Sorop, M. Evangelisti, M. Haase, and L. J. de Jongh, J. Magn. Magn. Mater. **272–276**, 1573 (2004).

[13] J. A. Mydosh, in *Spin Glasses: An Experimental Introduction* (Taylor & Francis, London, 1993).

[14] A. H. Cooke and J. G. Park, Proc. Phys. Soc. (London) **69**, 282 (1956).

[15] A. Abragam and B. Bleaney, *Electron Paramagnetic Resonance of Transition Ions* (Clarendon Press, Oxford, 1970).

[16] H. H. A. Smit, P. R. Nugteren, R. C. Thiel, and L. J. de Jongh, Physica B **153**, 33 (1988).

[17] P. M. Paulus, A. Goossens, R. C. Thiel, and A. M. van der Kraan, G. Schmid, and L. J. de Jongh, Phys. Rev. B **64**, 205418 (2001).

[18] See, e.g., M. Evangelisti, F. Luis, L. J. de Jongh, and M. Affronte, J. Mater. Chem. **16**, 2534 (2006).

[19] C. J. Ellis, M. J. M. Leask, D. M. Martin, and M. R. Wells, J. Phys. C **4**, 2937 (1971).

[20] N. A. Metropolis, A. W. Rosenbluth, M. N. Rosenbluth, A. H. Teller, and E. Teller, J. Chem. Phys. **21**, 1087 (1953).

[21] D. Bloch, J. Phys. Chem. Solids **27**, 881 (1966).

[22] R. J. Birgeneau, M. T. Hutchings, and W. P. Wolf, Phys. Rev. Lett. **17**, 308 (1966).

[23] R. W. Cochrane and W. P. Wolf, Solid State Commun. **9**, 1997 (1971).

[24] L. J. de Jongh and R. Block, Physica B **79**, 568 (1975).

[25] U. Bossek, K. Wieghardt, B. Nuber, and J. Weiss, Angew. Chem., Int. Ed. Engl. **29**, 1521 (1990).

[26] J. H. Colwell, B. W. Mangum, and D. D. Thornton, Phys. Rev. B **3**, 3855 (1971).

[27] P. Dalmas de Réotier and A. Yaouanc, J. Phys. Condens. Matter **9**, 9113 (1997).

[28] M. R. Crook and R. Cywinski, J. Phys. Condens. Matter **9**, 1149 (1997).

[29] The time scale of the μSR is of order $\lambda^{-1} \sim 1~\mu$s, corresponding to internal fields $B_{int} \approx 10$ mT, which should be fully decoupled for $B_{app} \geqslant 5 B_{int} \sim 50$ Oe already.

[30] T. Morya, Prog. Theor. Phys. **16**, 23 (1956); **16**, 641 (1956).

[31] R. I. Bewley and R. Cywinski, Phys. Rev. B **58**, 11544 (1998).

[32] E. M. Forgan, T. J. Jackson, T. M. Riseman, H. Glückler, E. Morenzoni, T. Prokscha, H. P. Weber, A. Hofer, C. Niedermayer, G. Schatz, M. Birke, H. Luetkens, J. Litterst, A. Schatz, and C. Binns, Physica B **289-290**, 137 (2000); T. J. Jackson, C. Binns, E. M. Forgan, E. Morenzoni, Ch. Niedermayer, H. Glückler, A. Hofer, H. Luetkens, T. Prokscha, T. M. Riseman, A. Schatz, M. Birke, J. Litterst, G. Schatz, and H. P. Weber, J. Phys. Condens. Matter **12**, 1399 (2000).

[33] S. J. Blundell, I. M. Marshall, W. Hayes, and F. L. Pratt, Phys. Rev. B **70**, 212408 (2004).

[34] Y. J. Uemura, T. Yamazaki, D. R. Harshman, M. Senba, and E. J. Ansaldo, Phys. Rev. B **31**, 546 (1985).

[35] Since the exchange frequency $\omega_{ex} \approx 2 \times 10^{11}$ for Dy^{3+} is so much larger, its contribution to λ is too small to be considered.

[36] D. W. Forester and W. A. Fernando, Phys. Rev. B **13**, 3991 (1976).

[37] M. J. Metcalfe and H. M. Rosenberg, Phys. Lett. A **33**, 211 (1970).

[38] A. H. Cooke and J. D. Cashion, J. Phys. C **12**, 605 (1979).

[39] K. V. Loftus, M. W. S. Parsons, H. M. Rosenberg, S. J. Swithenby, and M. R. Wells, Phys. Lett. A **45**, 471 (1973).

[40] B. Bleaney, A. C. de Oliveira, and M. R. Wells, J. Phys. C: Solid State Phys. **15**, 5305 (1982).

[41] J. D. Cashion, A. H. Cooke, L. A. Hoel, D. M. Martin, and M. R. Wells, Proc. Colloq. Intern. CNRS Eléments des Terres Rares **180**, 417 (1970).